

1 Correlative all-optical quantification 2 of mass density and mechanics of 3 sub-cellular compartments with 4 fluorescence specificity

5 **Raimund Schlüßler**^{1,*†}, **Kyoohyun Kim**^{1,2,*†}, **Martin Nötzel**¹, **Anna**

6 **Taubenberger**¹, **Shada Abuhattum**^{1,2}, **Timon Beck**^{1,2}, **Paul Müller**^{1,2},

7 **Shovamayee Maharana**^{1,3}, **Gheorghe Cojoc**¹, **Salvatore Girardo**^{1,2},

8 **Andreas Hermann**⁴, **Simon Alberti**^{1,5}, **Jochen Guck**^{1,2,5,*}

*For correspondence:

raimund.schlüssler@tu-dresden.de (RS);

kyoohyun.kim@mpl.mpg.de (KK);

jochen.guck@mpl.mpg.de (JG)

†These authors contributed
equally to this work

9 ¹Biotechnology Center, Center for Molecular and Cellular Bioengineering,
Technische Universität Dresden, 01307 Dresden, Germany; ²Max Planck
10 Institute for the Science of Light and Max-Planck-Zentrum für Physik und
Medizin, 91058 Erlangen, Germany; ³Department of Microbiology and
11 Cell Biology, Indian Institute of Science, 560012 Bengaluru, India;
12 ⁴Translational Neurodegeneration Section "Albrecht Kossel", University
13 Rostock, and German Center for Neurodegenerative Diseases (DZNE),
14 Rostock/Greifswald, 18147 Rostock, Germany; ⁵Physics of Life,
15 Technische Universität Dresden, 01307 Dresden, Germany

16

17

18

19 **Abstract** Quantitative measurements of physical parameters become increasingly
20 important for understanding biological processes. Brillouin microscopy (BM) has
21 recently emerged as one technique providing the 3D distribution of viscoelastic
22 properties inside biological samples — so far relying on the implicit assumption that
23 refractive index (RI) and density can be neglected. Here, we present a novel method
24 (FOB microscopy) combining BM with optical diffraction tomography and
25 epi-fluorescence imaging for explicitly measuring the Brillouin shift, RI and absolute
26 density with specificity to fluorescently labeled structures. We show that neglecting the
27 RI and density might lead to erroneous conclusions. Investigating the nucleoplasm of
28 wild-type HeLa cells, we find that it has lower density but higher longitudinal modulus
29 than the cytoplasm. Thus, the longitudinal modulus is not merely sensitive to the water
30 content of the sample — a postulate vividly discussed in the field. We demonstrate the
31 further utility of FOB on various biological systems including adipocytes and
32 intracellular membraneless compartments. FOB microscopy can provide unexpected
33 scientific discoveries and shed quantitative light on processes such as phase separation
34 and transition inside living cells.

35

36 Introduction

37 The mechanical properties of tissues, single cells, and intracellular compartments are
38 linked to their function, in particular during migration and differentiation, and as a re-
39 sponse to external stress (Engler *et al.*, 2006; Provenzano *et al.*, 2006; Lo *et al.*, 2000).
40 Hence, characterizing mechanical properties *in vivo* has become important for under-
41 standing cell physiology and pathology, e.g. during development or cancer progression
42 (Mammoto *et al.*, 2013; Jansen *et al.*, 2015; Mohammed *et al.*, 2019). To measure the
43 mechanical properties of biological samples, many techniques are available. These in-
44 clude atomic force microscopy (Christ *et al.*, 2010; Koser *et al.*, 2015; Gautier *et al.*, 2015;
45 Franze *et al.*, 2013), micropipette aspiration (Maître *et al.*, 2012), and optical traps (Wu
46 *et al.*, 2018a; Litvinov *et al.*, 2002; Bambadekar *et al.*, 2015; Guck *et al.*, 2001). These
47 techniques can access the rheological properties of a sample and their changes under
48 various pathophysiological conditions. Yet, most of them require physical contact be-
49 tween probe and sample surface and none of them allows to obtain spatially resolved
50 distributions of the mechanical properties inside the specimens.

51 Brillouin microscopy has emerged as a novel microscopy technique to provide label-
52 free, non-contact, and spatially resolved measurements of the mechanical properties
53 inside biological samples (Scarcelli and Yun, 2008; Scarcelli *et al.*, 2015; Antonacci *et al.*,
54 2018; Prevedel *et al.*, 2019). The technique is based on Brillouin light scattering which
55 arises from the inelastic interaction between the incident photons and collective fluctua-
56 tions of the molecules (acoustic phonons) (Brillouin, 1922; Boyd, 2008). The Brillouin shift
57 measured is related to the longitudinal modulus, refractive index (RI), and absolute den-
58 sity and the Brillouin peak linewidth is associated with the viscosity of the sample (see
59 Methods). The longitudinal modulus characterizes the compressibility of a sample and is
60 in the GPa range for common biological samples (Prevedel *et al.*, 2019). While the longi-
61 tudinal modulus is theoretically related to the more commonly used Young's modulus by
62 the Poisson's ratio, a conversion between the two moduli is generally not possible, since
63 the Poisson's ratio is frequency dependent and normally unknown. However, multiple
64 studies found empirical correlations between the longitudinal modulus and the Young's
65 modulus (Scarcelli *et al.*, 2011, 2015; Schlüßler *et al.*, 2018). Furthermore, the longitu-
66 dinal modulus takes into account all instrument properties like wavelength or scattering
67 angle, and does not need normalization for comparability between different setups as
68 the Brillouin shift does (Antonacci *et al.*, 2020). So far, conventional Brillouin microscopy
69 does not consider the contribution of heterogeneous RI and absolute density distribu-
70 tions to the longitudinal modulus. Most studies either assume a homogeneous RI distri-
71 bution (Scarcelli and Yun, 2008; Scarcelli *et al.*, 2011; Antonacci and Braakman, 2016),
72 argument that the RI and absolute density trivially cancel out (Scarcelli *et al.*, 2012, 2015;
73 Antonacci *et al.*, 2018) or use RI values obtained separately by other imaging setups
74 (Schlüßler *et al.*, 2018). Other approaches to calculate the longitudinal modulus mea-
75 sure the mass density of the sample, but still rely on a priori knowledge of the RI (Liu
76 *et al.*, 2019; Remer *et al.*, 2020). These simplifications may result in an inaccurate calcu-
77 lation of the longitudinal modulus, since the RI distribution might not be homogenous
78 throughout the sample, RI and density might not be coupled, hence, not cancel out, or
79 the sample preparations necessary for separate RI measurements could influence the
80 RI measured. Only recently, serial Brillouin measurements of samples illuminated under
81 different illumination angles allowed measuring the RI value inside the focal volume as

82 well (**Fiore, 2019**). However, this technique requires illuminating the sample from two
83 different directions, which doubles the acquisition time and decreases the spatial reso-
84 lution of the measurement when compared to a setup only acquiring the Brillouin shift.

85 Optical diffraction tomography (ODT) has been utilized for measuring the three-di-
86 mensional (3D) RI distribution of various specimens (**Sung et al., 2009; Cotte et al., 2013;**
87 **Kim et al., 2016a**). Employing quantitative phase imaging, ODT can reconstruct the 3D RI
88 distribution of living biological samples from the complex optical fields measured under
89 different illumination angles. Given the RI, the mass density and protein concentration
90 of most biological samples can be calculated using a two-substance mixture model (see
91 Methods) (**Barer, 1952; Popescu et al., 2008; Zangle and Teitell, 2014**). Protein concentra-
92 tions acquired with ODT were shown to agree well with results from volume-based mea-
93 surements and did not suffer from differences in the quantum yield of fluorescent dyes
94 between dilute and condensed phase as it might happen for fluorescence intensity ratio
95 measurements (**McCall et al., 2020**). However, using the two-substance mixture model
96 requires knowledge of the refraction increment, which depends on the material compo-
97 sition and takes on values of 0.173 ml/g to 0.215 ml/g with an average of 0.190 ml/g for dif-
98 ferent human proteins (**Zhao et al., 2011; Theisen, 2000**) and can go down to 0.135 ml/g to
99 0.138 ml/g for phospholipids (**Erbe and Sigel, 2007; Mashaghi et al., 2008**). Furthermore,
100 the two-substance mixture model does not apply to cell compartments mainly filled with
101 a single substance, e.g. lipid droplets in adipocytes. Hence, specificity by e.g. fluo-
102 rescence imaging is necessary to determine whether the two-substance mixture model is
103 appropriate and which refraction increment should be used to calculate the absolute
104 density of a certain cell region.

105 Here, we present a combined optical system for epi-fluorescence, ODT, and Brillouin
106 microscopy (FOB microscopy) which can provide the correct longitudinal modulus from
107 colocalized measurements of the Brillouin shift and RI distributions and the subsequently
108 calculated absolute densities of a sample. The principal function of the FOB microscope is
109 demonstrated by measurements of cell phantoms made of biconstituent polymers with
110 known mechanical properties. We further applied the setup to HeLa cells and adipocytes.
111 First, we investigated two condensates that form by physical process of phase separa-
112 tion – nucleoli in the nucleus and stress granules (SGs) in the cytoplasm (**Alberti and**
113 **Dormann, 2019**). Nucleoli in HeLa cells showed a higher RI ($n = 1.3618 \pm 0.0004$) and lon-
114 gitudinal modulus ($M' = 2.487 \pm 0.005$ GPa) than the cytoplasm ($n = 1.3545 \pm 0.0004, M' =$
115 2.410 ± 0.005 GPa), whereas the nucleoplasm had a lower RI ($n = 1.3522 \pm 0.0004$) than the
116 cytoplasm while still showing a higher longitudinal modulus ($M' = 2.448 \pm 0.005$ GPa). The
117 RI of the cytoplasm and nucleoplasm decreased after stressing HeLa cells with arsen-
118 ite, but we found no statistically significant difference of either the RI or longitudinal
119 modulus of SGs to the surrounding cytoplasm. By contrast, poly-Q aggregates formed
120 by overexpressing the aggregation-prone exon 1 of Q103 huntingtin exhibited a 2.5%
121 higher RI and 20.0 % higher longitudinal modulus compared to the surrounding compart-
122 ment. Moreover, unlike water-based cellular condensates and aggregates, lipid droplets
123 inside adipocytes showed higher RI and Brillouin shift, but lower longitudinal modulus
124 than the cytoplasm when taking into account their absolute density. These data illus-
125 trates that in order to correctly calculate the longitudinal modulus, the RI as well as the
126 absolute density have to be taken into account. In summary, the presented setup could
127 provide measurement data necessary for a deeper understanding of pathophysiological

128 processes related to cell mechanics and condensates that form by the process of phase
129 separation.

130 **Results**

131 **Optical setup**

132 FOB microscopy combines ODT with Brillouin microscopy and epi-fluorescence imaging
133 (Figure 1a). The three imaging modalities are sequentially applied to quantitatively map
134 the RI, the Brillouin shift, and the epi-fluorescence intensity distribution inside a given
135 sample. These parameters allow to e.g. infer the mass density and dry mass of the sam-
136 ple, and provide specificity to fluorescently labeled structures. Given the fluorescence
137 specificity, it is furthermore possible to localize subcellular organelles of interest and to
138 determine whether for a certain region the two-substance mixture model can be applied
139 to calculate the local absolute density, or if the literature value of the absolute density
140 has to be used (e.g. in lipid droplets). Finally, with the combination of RI, absolute density,
141 and Brillouin shift distributions, the longitudinal modulus can be calculated.

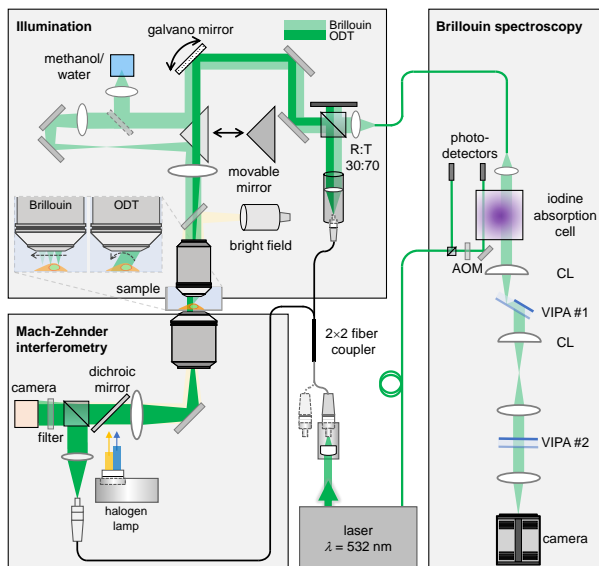
142 For ODT, the sample is illuminated with a plane wave under different incident angles.
143 To illuminate the sample under different angles, a dual-axis galvanometer mirror tilts the
144 illumination beam. The transmitted light interferes with a reference beam and creates a
145 spatially modulated hologram on a camera from which the phase delay and finally the RI
146 of the sample is calculated with a resolution of $0.25\text{ }\mu\text{m}$ within the lateral plane and $0.5\text{ }\mu\text{m}$
147 in the axial direction (Figure 1c). Epi-fluorescence microscopy captures the fluorescence
148 emission intensity image (Figure 1b) with the same camera used for the ODT acquisition.

149 For Brillouin microscopy, a moveable mirror guides the incident light to an additional
150 lens which leads to a focus in the sample with a size of $0.4\text{ }\mu\text{m}$ in the lateral plane and
151 approximately $1\text{ }\mu\text{m}$ in axial direction. The focus is translated by the galvanometer mirror
152 to scan the whole sample. The Brillouin scattered light is collected in the backscattering
153 configuration and guided to a two-stage virtually imaged phased array (VIPA) spectrome-
154 ter (*Scarcelli and Yun, 2008*). The Brillouin shift (Figure 1d) is extracted from the recorded
155 Brillouin spectrum and the longitudinal modulus (Figure 1e) is calculated from the Bril-
156 louin shift, RI and absolute density distributions acquired (see Methods).

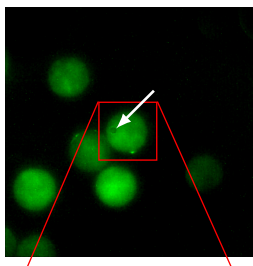
157 **Validation of the setup with cell phantoms**

158 To validate the basic performance of the combined FOB microscopy setup, we acquired
159 the RI and Brillouin shift of an artificial cell phantom with known material properties. The
160 phantom consists of a polydimethylsiloxane (PDMS) bead embedded in a polyacrylamide
161 (PAA) bead (Figure 1b-e) which was fluorescently labeled with Alexa 488 (See Methods).
162 The material properties of the two components of the phantom are expected to be homo-
163 geneous, so that the standard deviation (SD) of the values measured can be used as an
164 estimate of the setups measurement uncertainty. The RI of the embedded PDMS bead
165 was measured as 1.3920 ± 0.0080 (mean value \pm SD) (Figure 1c). This was slightly lower
166 than values reported for bulk PDMS with the RI of 1.416 (*Meichner et al., 2015*), which
167 could be due to the swelling of the PDMS beads during the fabrication process (*Wang*
168 *et al., 2015*). The RI of the PAA bead (1.3485 ± 0.0024) was substantially lower than that
169 of the PDMS bead, and was close to the previously reported value (*Girardo et al., 2018*).
170 In contrast, the Brillouin shift of the PDMS bead ($7.279 \pm 0.043\text{ GHz}$) was lower than for

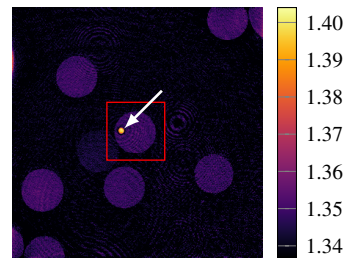
a) Optical setup



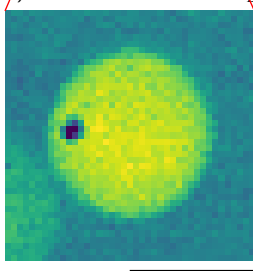
b) Fluorescence intensity



c) Refractive index



d) Brillouin shift



e) Longitudinal modulus M' [GPa]

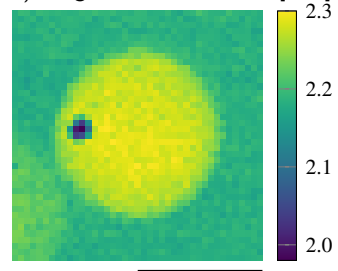


Figure 1. Combined fluorescence, optical diffraction tomography (ODT) and Brillouin microscopy. (a) Optical setup. The beam paths for epi-fluorescence / brightfield imaging, ODT and Brillouin microscopy are shown in light yellow, dark green and light green, respectively. The laser light illuminating the sample is collimated in ODT mode and focused in Brillouin mode. A moveable mirror enables to switch between the two modes. The Brillouin scattered light is guided to the spectrometer by a single-mode fiber, which acts as confocal pinhole. The light transmitted through the sample interferes with a reference beam. AOM, acousto-optic modulator; CL, cylindrical lens; LED, light-emitting diode; VIPA, virtually imaged phased array. (b-e) Quantitative and spatially resolved maps of a cell phantom consisting of a PDMS bead (indicated by the white arrows) inside a PAA bead stained with Alexa 488 (green fluorescence in (b)) acquired with the FOB microscope. (b) epi-fluorescence intensities, (c) refractive indices, (d) Brillouin shifts and (e) calculated longitudinal moduli. The size of the Brillouin map is 41 by 41 pixel, resulting in an acquisition duration of 30 min. Scale bars 10 μ m.

The following figure supplements are available for figure 1:

Figure supplement 1. Absolute density of a cell phantom consisting of a PDMS bead inside a PAA bead. Scale bar 10 μ m.

171 the PAA bead (7.574 ± 0.020 GHz) (Figure 1d). In order to calculate the longitudinal mod-
172 ulus, the absolute density of the PAA bead (1.019 ± 0.001 g/ml) was calculated from the
173 measured RI by applying a two-substance mixture model (See Methods). However, this
174 model cannot be applied for the PDMS bead, since the bead does not contain a fluid
175 phase. Hence, the area of the PDMS bead was segmented based on the RI and fluo-
176 rescence intensity (Figure 1b), and the literature value for the absolute density of PDMS
177 (1.03 g/ml) was used (see Figure 1-figure supplement 1) (*Rahman et al., 2012*). The result-
178 ing longitudinal modulus is shown in Figure 1e. We found values of 2.022 ± 0.030 GPa for
179 the PDMS bead and 2.274 ± 0.012 GPa for the PAA bead. The results are consistent with
180 previous measurements of the speed of sound in PDMS (*Cafarelli et al., 2017*) and the
181 longitudinal modulus of PAA (*Schlüßler et al., 2018*) when taking into account the abso-
182 lute density of the dry fraction (i.e. (2)). Our finding clearly demonstrates the strength
183 of the presented FOB setup to provide local RI and absolute density distributions for
184 correctly calculating longitudinal modulus from the Brillouin shift measured.

185 **Cell nucleoplasm has lower absolute density but higher longitudinal
186 modulus than cytoplasm**

187 The FOB microscope can also provide much needed quantitative insight into a biologi-
188 cal phenomenon that has recently captured the imagination of physicists and biologists
189 alike – the formation of membraneless compartments by liquid-liquid phase separation
190 (LLPS) (*Brangwynne et al., 2011*). One such membraneless compartment is the nucle-
191 olus, a region within the nucleus where ribosomal subunits are synthesized. Here, we
192 recorded the epi-fluorescence, Brillouin shift, and RI distributions of 139 HeLa cells in
193 which a nucleolar marker protein NIFK was tagged with GFP and the nuclei were stained
194 with Hoechst (See Methods). In order to evaluate the mechanical properties of the cyto-
195 plasm, nucleoplasm, and nucleoli separately, we segmented the different compartments
196 of the cells based on the RI and the two-channel epi-fluorescence intensity maps (Fig-
197 ure 2a, see Methods).

198 As shown in Figure 2b and d, the nucleoplasm of HeLa cells exhibited a statistically
199 significantly lower RI than the cytoplasm (Kruskal-Wallis $p_{n_{cyto},n_{np}} = 9 \times 10^{-4}$), with values of
200 1.3522 ± 0.0004 (mean value \pm SEM) (nucleoplasm) and 1.3545 ± 0.0004 (cytoplasm), which
201 is consistent with previous studies (*Schürmann et al., 2016; Kim and Guck, 2020*). Since
202 the RI of the HeLa cells measured is linearly proportional to their mass density (*Kim and
203 Guck, 2020*), we applied the two-substance mixture model and used a global refraction
204 increment of 0.190 ml/g, which is valid for protein and nucleic acid (*Zhao et al., 2011;
205 Zangle and Teitell, 2014*), to calculate the absolute densities of each cell and its compart-
206 ments. The resulting absolute densities are shown in Figure 2-figure supplement 1b and
207 d. We found that the nucleoplasm had a lower absolute density (1.0207 ± 0.0005 g/ml) than
208 the cytoplasm (1.0234 ± 0.0006 g/ml). Here, the perinuclear cytoplasm also contains many
209 lipid-rich membrane-bound organelles, and the RI increment of phospholipids (0.135 ml/g
210 to 0.138 ml/g, (*Erbe and Sigel, 2007; Mashaghi et al., 2008*)) is lower than that of protein
211 and nucleic acid. Hence, the calculated absolute density of the cytoplasm could be un-
212 derestimated and the absolute density difference between cytoplasm and nucleoplasm
213 might be even more pronounced.

214 Interestingly, the Brillouin shift of the nucleoplasm (7.872 ± 0.007 GHz) was statistically
215 significantly higher than the value of the cytoplasm (7.811 ± 0.008 GHz)

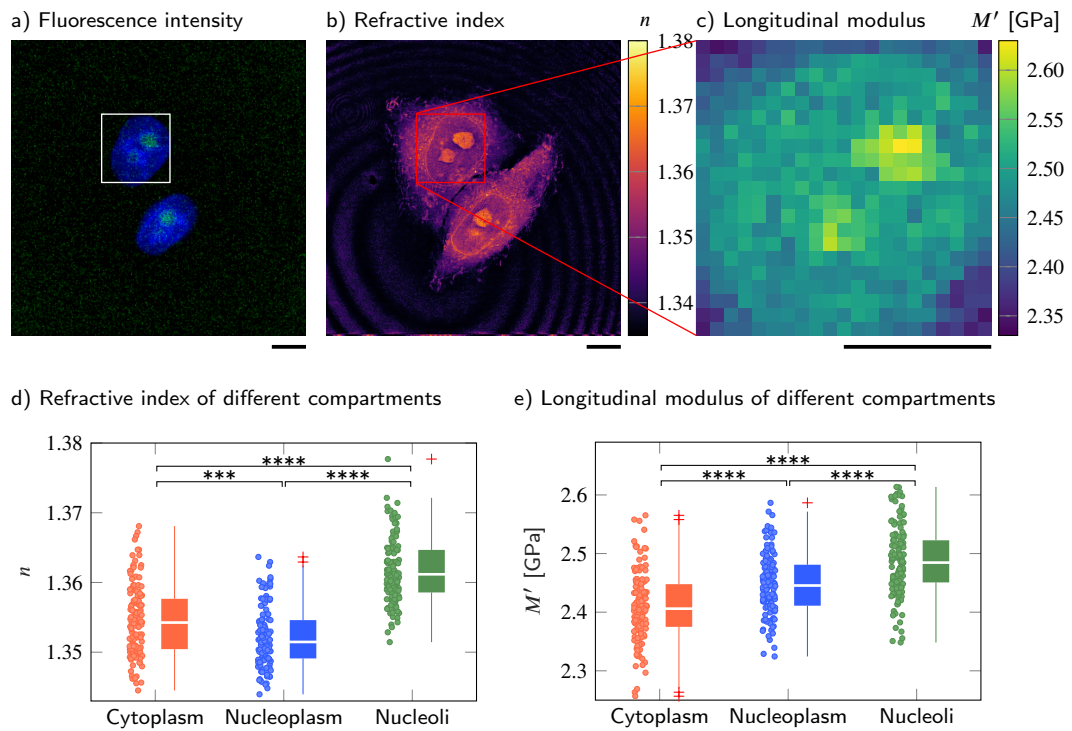


Figure 2. Cell nucleoplasm has lower RI but higher longitudinal modulus than cytoplasm. **(a-c)** Representative maps of the **(a)** epi-fluorescence intensity distribution, **(b)** longitudinal moduli and **(c)** refractive indices of a HeLa cell. Nuclei are stained with Hoechst (blue) and the nucleolar protein in the nucleoli is labeled with GFP (green). Quantitative analysis of **(d)** the refractive index and **(e)** the calculated longitudinal modulus taking into account the Brillouin shifts, refractive indices and absolute densities of 139 HeLa cells. The size of the Brillouin map is 21 by 21 pixel, resulting in an acquisition duration of 8 min. Scale bars 10 μ m. *** p < 0.001; **** p < 0.0001. The following figure supplements are available for figure 2:

Figure supplement 1. Brillouin shift and absolute density of cytoplasm, nucleoplasm and nucleoli in HeLa cells. Representative maps of the **(a)** Brillouin shift and **(b)** absolute density of a HeLa cell. Quantitative analysis of **(c)** the Brillouin shift v_B , **(d)** the absolute density ρ and **(e)** peak linewidth Δ_B . ** p < 0.01; **** p < 0.0001. Scale bars 10 μ m.

Source data 1. Refractive index, longitudinal modulus, Brillouin shift and absolute density values of different compartments in HeLa cells.

Supplementary File 1 Average values and standard errors of the mean of the RI n , Brillouin shift v_B , absolute density ρ , longitudinal modulus M' and linewidths Δ_B for the cytoplasm (cyto), nucleoplasm (np) and nucleoli (nl) of 139 wild-type HeLa cells.

Supplementary File 2 Kruskal-Walis p -values when comparing the RI n , Brillouin shifts v_B , mass densities ρ , longitudinal moduli M' and linewidths Δ_B of the cytoplasm (cyto), nucleoplasm (np) and nucleoli (nl) of 139 wild-type HeLa cells, respectively.

²¹⁶ $(p_{v_{B, \text{cyto}}, v_{B, \text{np}}} = 2 \times 10^{-6}$, Figure 2-figure supplement 1a and d). The longitudinal moduli of
²¹⁷ the nucleoplasm (2.448 ± 0.005 GPa) and cytoplasm (2.410 ± 0.005 GPa) followed the same
²¹⁸ trend as the Brillouin shifts ($p_{M'_{\text{cyto}}, M'_{\text{np}}} = 7 \times 10^{-7}$, Figure 2c and e). Moreover, the nucle-

219 oli, where ribosomal subunits are synthesized, exhibited statistically significantly higher
220 RI ($n = 1.3618 \pm 0.0004$), Brillouin shift ($v_B = 7.938 \pm 0.008$ GHz), and longitudinal modulus
221 ($M' = 2.487 \pm 0.005$ GPa) than either nucleoplasm or cytoplasm. We further found that
222 the Brillouin peak linewidth of the cyto- and nucleoplasm is not statistically significantly
223 different, but shows a statistically significant increase in the nucleoli (Figure 2-figure sup-
224 plement 1e). This indicates a higher viscosity and a less fluid-like behaviour in the nucle-
225 oli compared to the cyto- and nucleoplasm. A full list of the resulting RI, Brillouin shifts,
226 absolute densities, longitudinal moduli and linewidths and the corresponding *p*-values
227 when comparing between different cell compartments can be found in the Supplemen-
228 tary Files 1 and 2.

229 These findings imply that membraneless compartments formed by phase separation,
230 in this case the nucleolus, can maintain a higher absolute density and distinct compres-
231 sibility (here, higher longitudinal modulus) in spite of the thermodynamic instability inher-
232 ent in this state.

233 **PolyQ aggregates have higher absolute density and longitudinal mod-
234 ulus than cytoplasm**

235 To compare the properties of physiological condensates with a densely packed protein
236 aggregate, we overexpressed an expanded version of the aggregation-prone exon 1 of
237 huntingtin with 103 consecutive glutamines (*Lieberman et al., 2019; Norrbacka et al.,
238 2019; Bäuerlein et al., 2017*). Q103 phase separates into liquid droplets in cells and these
239 droplets rapidly convert into a solid-like state (*Yang and Yang, 2020*), meaning they do
240 not recover from photobleaching when subjected to fluorescence recovery after photo-
241 bleaching (FRAP) experiments (*Kroschwald et al., 2015*). Here, we observe polyglutamine
242 (polyQ) aggregates labeled with GFP in transiently transfected wild-type HeLa cells. We
243 used the FOB microscope to measure the mechanical properties of polyQ granules in
244 22 different cells.

Supplementary File 3 Average values and standard errors of the mean of the RI n , Brillouin shift
 v_B , absolute density ρ and longitudinal modulus M' for the cytoplasm and polyQ aggregates of 22
wild-type HeLa cells.

245 The polyQ aggregates showed a strong fluorescence signal in the GFP channel (Figure
246 3a). We hence used the fluorescence intensity to segment the aggregates from the
247 peripheral cytoplasm in order to quantitatively compare cytoplasm and aggregates (Figure
248 3b and c). The RI (1.3856 ± 0.0018) and the longitudinal modulus (3.051 ± 0.029 GPa) of
249 the aggregates were statistically significantly higher ($p < 0.0001$) than the RI (1.3506 ± 0.0013)
250 and longitudinal modulus (2.442 ± 0.009 GPa) of the peripheral cytoplasm (Figure 3d and
251 f and Supplementary File 3). Using the RI measured, we find a protein concentration of
252 255.8 ± 9.4 mg/ml in the polyQ aggregates, a 4-fold higher concentration than the value of
253 65 mg/ml previously measured with ODT in a G3BP1 *in vitro* system (*Guillén-Boixet et al.,
254 2020*). Our results show that FOB microscopy can quantify the physical properties of
255 cytoplasmic membraneless condensates – in principle.

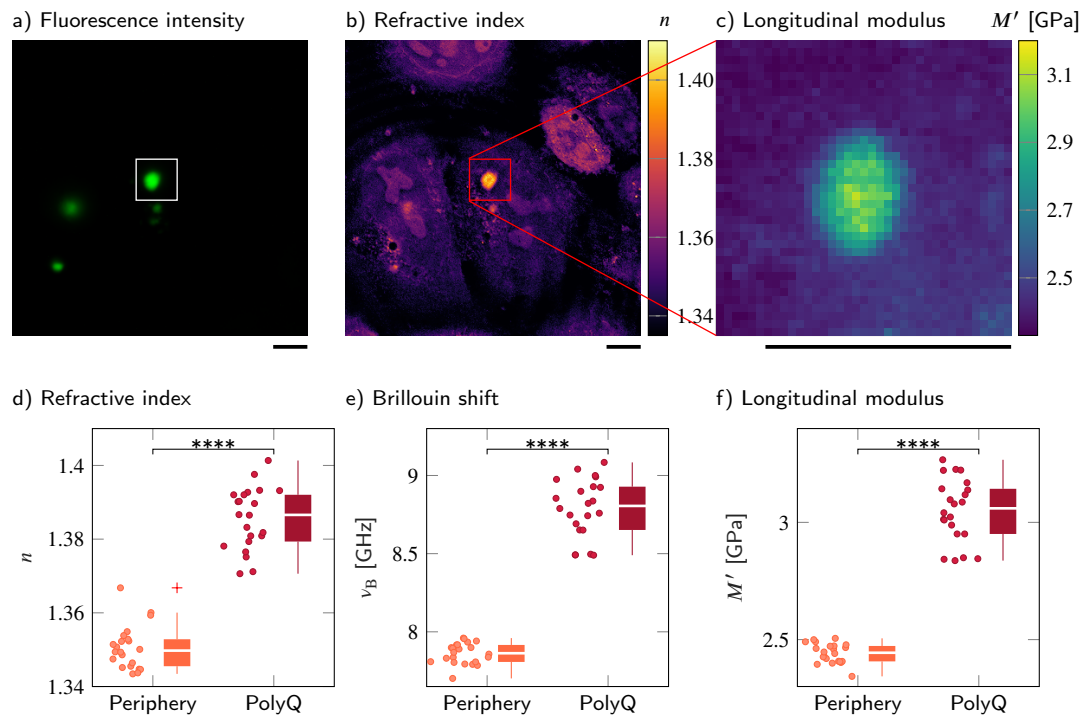


Figure 3. PolyQ aggregates have a higher refractive index, Brillouin shift and longitudinal modulus than the peripheral cytoplasm. **(a-c)** Representative maps of **(a)** the epi-fluorescence intensity distribution, **(b)** the refractive indices and **(c)** the longitudinal moduli of a HeLa cell transfected with a plasmid encoding HttQ103. The polyQ aggregates are labeled with GFP (green). Quantitative analysis of **(d)** the refractive index, **(e)** the Brillouin shift and **(f)** the calculated longitudinal modulus taking into account the Brillouin shifts, refractive indices and absolute densities of 22 polyQ granules. The size of the Brillouin map is 37 by 37 pixel, resulting in an acquisition duration of 23 min. Scale bars 10 μ m. *** $p < 0.0001$.

Source data 1. Refractive index, Brillouin shift and longitudinal modulus values of polyQ aggregates and their periphery.

256 **FUS-GFP stress granules in living P525L HeLa cells show RI and longi- 257 **tudinal modulus similar to the surrounding cytoplasm****

258 Recently, another type of condensates formed by LLPS — RNA and protein (RNP) gran-
259 ules, such as SGs — has received much attention, due to its linkage to neurodegenerative
260 diseases such as amyotrophic lateral sclerosis (ALS) and frontotemporal dementia (*Patel*
261 *et al.*, 2015; *Alberti and Hyman*, 2016). It is also increasingly recognized that the me-
262 chanical properties of these compartments influence their functions and involvement
263 in disease (Jawerth, 2018; Nötzel *et al.*, 2018). Fused in sarcoma (FUS) protein, an RNA-
264 binding protein involved in DNA repair and transcription, is one example of a protein
265 that localizes to SGs (*Patel et al.*, 2015). Purified FUS protein is able to phase separate
266 into liquid condensates in vitro, and this property is important for FUS to localize to SGs.
267 Disease-linked mutations in FUS have been shown to promote a conversion of reconsti-
268 tuted liquid FUS droplets from a liquid to a solid state, suggesting that an aberrant liquid
269 to solid transition of FUS protein promotes disease.

270 Conventionally, the mechanical changes of SGs have been indirectly characterized by
271 FRAP or observing fusion events of liquid droplets (*Brangwynne et al.*, 2009). Recently,

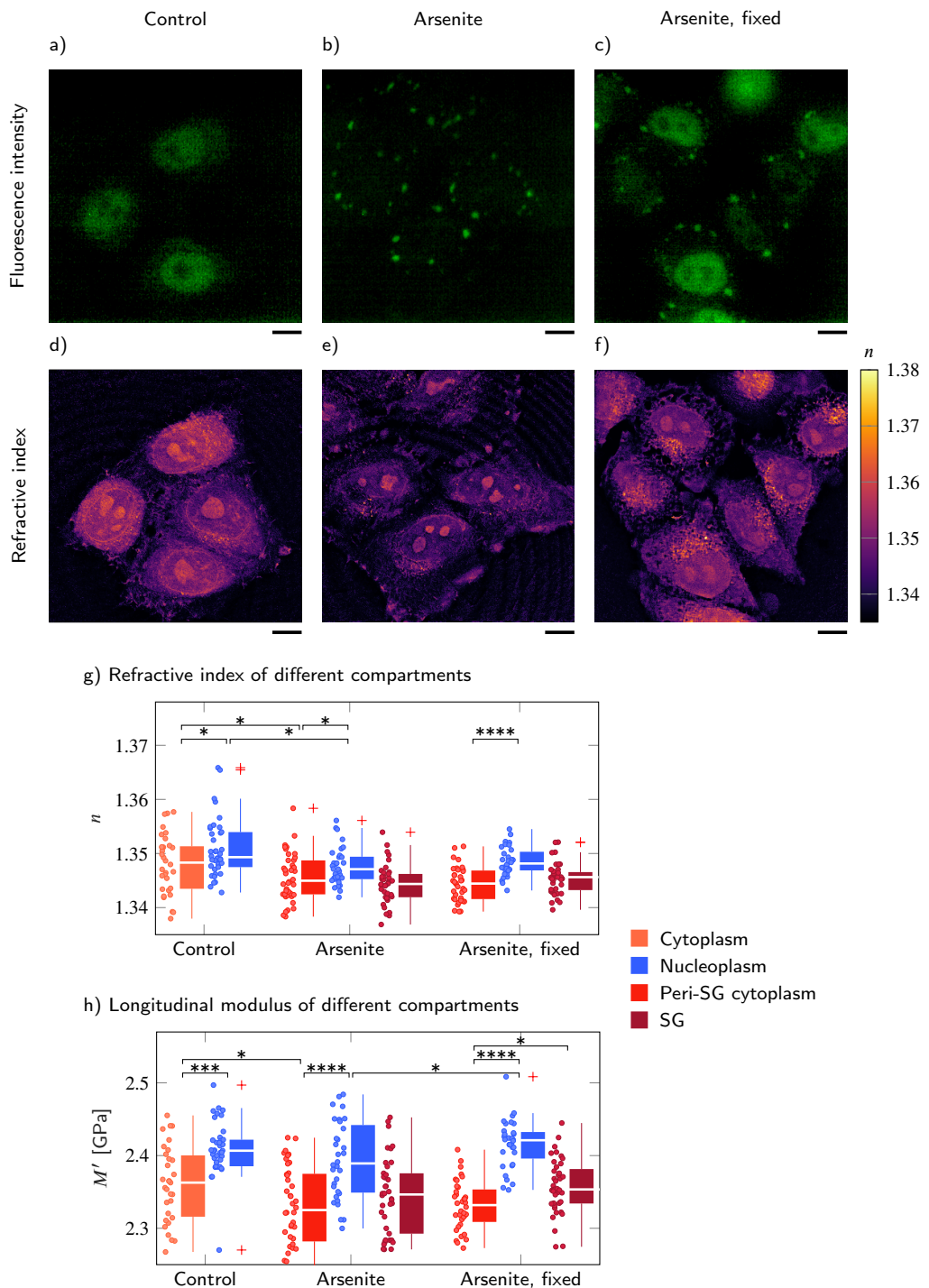


Figure 4. FUS-GFP-labelled stress granules induced by oxidative stress in living P525L FUS HeLa cells show a similar RI and longitudinal modulus as the peripheral cytoplasm. Representative example of (a-c) the fluorescence intensity and (d-f) the refractive index distribution under control conditions without arsenite, with arsenite, and with arsenite after fixation, respectively. Quantitative analysis of (g) the refractive index and (h) the calculated longitudinal modulus taking into account the Brillouin shift and refractive index. Scale bars 10 μ m. * $p < 0.05$; ** $p < 0.01$; *** $p < 0.001$; **** $p < 0.0001$.

The following figure supplements are available for figure 4:

Figure supplement 1. Comparison of the influence of different acquisition schemes and laser wavelengths on the viability of P525L HeLa cells which express GFP-tagged FUS. For better comparability the Brillouin shift v_B^* measured with the 780 nm setup is normalized to a wavelength of 532 nm. Scale bars 10 μ m.

Figure supplement 2. Evaluation of the RI of P525L FUS HeLa cells taking into account the complete cell. FUS-GFP-labelled stress granules induced by oxidative stress show a similar RI as the peripheral cytoplasm. * $p < 0.05$; *** $p < 0.0001$.

Source data 1. Refractive index and longitudinal modulus values of cytoplasm, nucleoplasm and SGs in P525L HeLa cells after different treatments.

272 Brillouin microscopy was used to measure the Brillouin shift of SGs in chemically fixed
273 P525L HeLa cells expressing mutant RFP-tagged FUS under doxycycline exposure (*An-*
274 *tonacci et al., 2018*). P525L HeLa cells are used as a disease model for ALS and form
275 SGs under arsenite stress conditions. It was shown that the Brillouin shift of SGs induced
276 by arsenite treatment with mutant RFP-FUS is statistically significantly higher than the
277 Brillouin shift of SGs without mutant RFP-FUS. Furthermore, the Brillouin shift of mutant
278 RFP-FUS SGs was reported to be statistically significantly higher than the value of the
279 surrounding cytoplasm (*Antonacci et al., 2018*).

280 Here, we applied the FOB setup to P525L HeLa cells which express GFP-tagged FUS,
281 and quantified the RI distributions, epi-fluorescence intensities, and Brillouin shifts of
282 the nucleoplasm, cytoplasm, and SGs. As not all HeLa cells were GFP-positive (see Fig-
283 ure 4a), we only selected the ones with a clear signal in the GFP channel. The cells were
284 measured under control conditions, after oxidative stress conditions when exposed to
285 5 mM sodium arsenite NaAsO₂ 30 min prior to the measurements and after chemical fix-
286 ation after oxidative stress. Since the SGs are not static, and assemble and disassemble
287 dynamically in living cells, acquiring the Brillouin shift map of a complete cell would be
288 to slow, which was the reason for the chemical fixation of the cells in a previous study
289 (*Antonacci et al., 2018*). During the approximate duration of 20 min to 30 min of a whole
290 cell measurement, SGs moved substantially or even disassembled and, hence, did not
291 colocalize with their epi-fluorescence signal acquired before. Furthermore, the P525L
292 FUS-GFP HeLa cells reacted sensitively to the exposure to green laser light and suffered
293 from cell death during a whole cell measurement. We therefore did not acquire Brillouin
294 shift maps of complete P525L HeLa cells, but only of small regions of 5 μ m by 5 μ m around
295 the SGs or the corresponding regions in the cytoplasm of the control cells. This reduced
296 the measurement duration to less than 2 min, allowing us to colocalize the SGs Brillouin
297 shift and epi-fluorescence signal and preventing cell death during the acquisition (see Fig-
298 ure 4—figure supplement 1). Hence, all measurements presented here stem from living
299 cells. The positions for the Brillouin shift measurements of the different compartments
300 were chosen manually based on the epi-fluorescence and brightfield intensities (see Fig-
301 ure 4a-f). In total, we measured over 100 different cells, with the number of values per
302 compartment and condition varying from 32 to 42, as shown in Figure 4g and h.

Supplementary File 4 Average values and standard errors of the mean of the RI n and
longitudinal modulus M' for different conditions and compartments of P525L HeLa cells.

303 We found that the RI of the cytoplasm measured in the region of SG formation was sta-
304 tistically significantly lower than the RI of the nucleoplasm for all conditions (control (c),
305 arsenite (a) and arsenite fixed (f)) tested ($p_c = 0.034$, $p_a = 0.035$, $p_f = 5 \times 10^{-6}$, Figure 4g
306 and Supplementary File 4). However, when segmenting the RI of the whole cell and
307 not only taking into account the RI of the manually selected regions for which we also
308 performed measurements of the Brillouin shift, we found a slightly, although not statis-
309 tically significantly, lower RI in the nucleoplasm than in the cytoplasm (Figure 4-figure
310 supplement 2). Hence, we think the higher RI of the nucleoplasm is a result of the man-
311 ual selection of the measurement positions in the region of SG formation near the cell
312 boundary. As for wild-type HeLa cells, the longitudinal modulus of the nucleoplasm was
313 statistically significantly higher than the modulus of the cytoplasm for all conditions ($p_c =$
314 1×10^{-4} , $p_a = 8 \times 10^{-6}$, $p_f = 1 \times 10^{-11}$, Figure 4h and Supplementary File 4). While the GFP-
315 tagged FUS of the control cells was mainly located in the nucleoplasm (Figure 4a), after
316 arsenite treatment the FUS was relocated from the nucleoplasm and aggregated in SGs
317 within the cytoplasm (Figure 4b). This was accompanied by a statistically significant de-
318 crease of the RI of both the peri-SG cytoplasm ($n_{a,peri-cyto} = 1.3456 \pm 0.0007$, $p = 0.019$) and
319 the nucleoplasm ($n_{a,nucleo} = 1.3476 \pm 0.0006$, $p = 0.017$) as well as of the longitudinal modu-
320 lus of the peri-SG cytoplasm ($M'_{a,peri-cyto} = 2.329 \pm 0.009$ GPa, $p = 0.036$). Furthermore, we
321 found no statistically significant difference of neither the RI ($n_{a,SG} = 1.3443 \pm 0.0006$) nor
322 the longitudinal modulus ($M'_{a,SG} = 2.345 \pm 0.009$ GPa) of SGs to the respective values in
323 the peri-SG cytoplasm. However, after chemical fixation the longitudinal modulus of the
324 SGs ($M'_{f,SG} = 2.357 \pm 0.006$ GPa) was statistically significantly higher than the longitudinal
325 modulus of the cytoplasm ($M'_{f,peri-cyto} = 2.331 \pm 0.006$ GPa, $p = 0.030$).

326 Altogether, in P525L HeLa cells expressing FUS-GFP the RI and longitudinal modulus
327 of the nucleoplasm of the control, arsenite treated, and fixed cells was statistically sig-
328 nificantly higher than the respective values in the cytoplasm. Interestingly, SGs showed
329 no statistically significant differences to the peri-SG cytoplasm in living, arsenite treated
330 cells, but had a statistically significantly higher longitudinal modulus in arsenite treated
331 and chemically fixed cells. This is consistent to previous studies showing a higher longi-
332 tudinal modulus of SGs compared to the cytoplasm in chemically fixed P525L HeLa cells
333 (*Antonacci et al., 2018*) and that fixation can substantially alter the mechanical (*Braet*
334 *et al., 1998*) as well as the optical properties (*Su et al., 2014*) of biological samples.

335 **Mechanical characterization of lipid droplets in adipocytes requires 336 precise RI and density**

337 Most biological cells can be thought of as a mixture of ions and macromolecules such
338 as proteins, nucleic acids, and sugars dissolved in water, for which the two-substance
339 mixture model (*Barer, 1952; Popescu et al., 2008; Zangle and Teitell, 2014*) is appropri-
340 ate to describe the relationship between the RI and the absolute density. However, this
341 is not the case for special compartments in certain cell types. The lipid droplets within
342 adipocytes are not composed of a water-based solution and cannot be characterized
343 by the two-substance mixture model. To overcome this problem, we exploit the speci-
344 ficity to fluorescently labeled structures of the FOB setup to identify and segment the
345 lipid droplets. Since previous mass spectroscopy studies on adipocyte cell culture mod-
346 els have identified palmitoyl triacylglycerides as predominant lipid species (*Gouw and*
347 *Vlugter, 1966; Liaw et al., 2016*), we use an absolute density value of 0.8932 g/ml for cal-

348 calculating the longitudinal moduli of the lipid droplets.

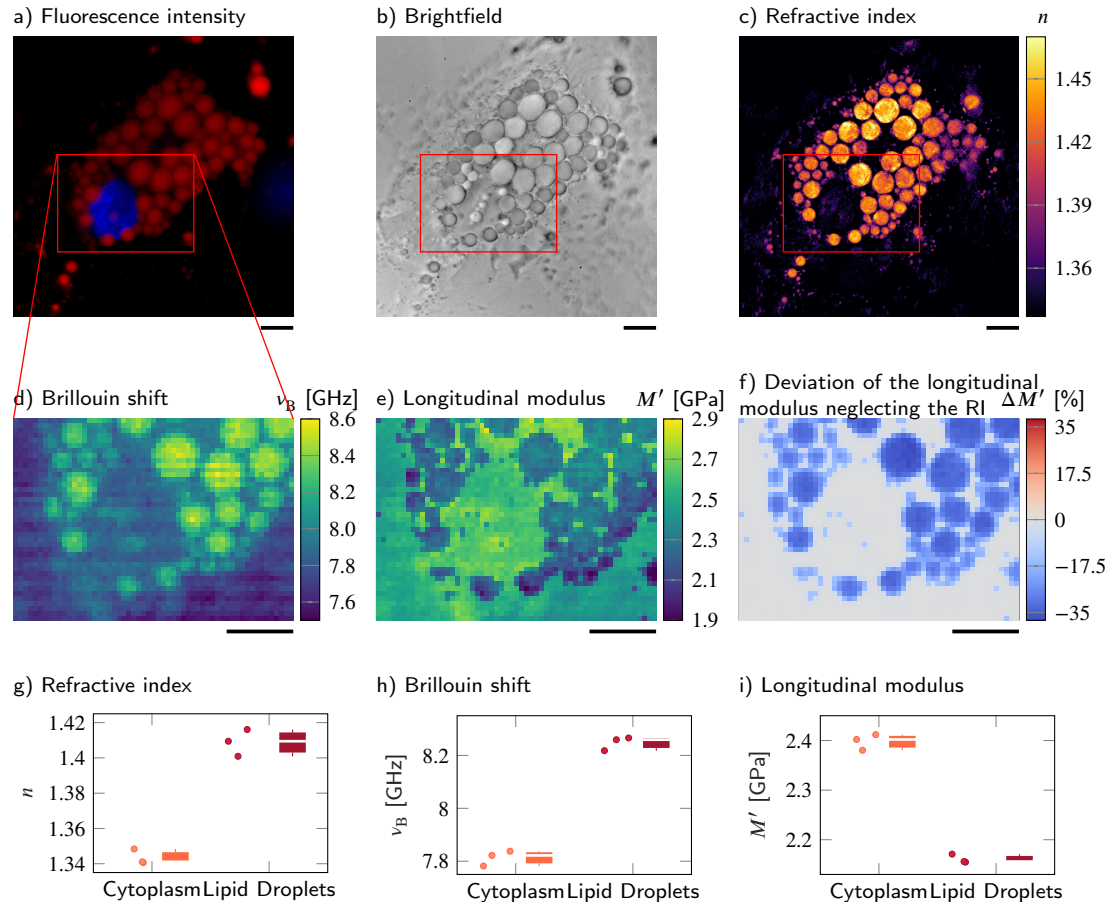


Figure 5. Despite a higher RI and Brillouin shift, the longitudinal modulus of lipid droplets is lower than of the surrounding cytoplasm. **(a-d)** Representative maps of the **(a)** epi-fluorescence intensities, **(b)** brightfield intensities, **(c)** refractive indices and **(d)** Brillouin shifts of an adipocyte cell. The nucleus is stained with Hoechst (blue in **(a)**) and lipid droplets are stained with Nile red (red in **(a)**). **(e)** Longitudinal modulus calculated from the refractive indices, absolute densities and Brillouin shifts. **(f)** Deviation of the longitudinal modulus calculated with a homogeneous refractive index and absolute density value when compared to the precise longitudinal modulus in **(e)**. Quantitative analysis of **(g)** the refractive index, **(h)** the Brillouin shift and **(i)** the calculated longitudinal modulus taking into account the Brillouin shifts, refractive indices and absolute densities of $N = 3$ adipocytes. The size of the Brillouin map is 57 by 41 pixel, resulting in an acquisition duration of 40 min. Scale bar 10 μ m

349 Here, we observed Simpson-Golabi-Behmel Syndrome (SGBS) adipocytes (**Wabitsch**
 350 **et al., 2001**) ($N = 3$) whose nucleus and lipid droplets were stained with Hoechst and
 351 Nile red respectively on day 11 of adipogenic differentiation. The lipid droplets were
 352 clearly visible in the fluorescence intensity (Figure 5a) and showed a high mean RI value of
 353 1.409 ± 0.004 (Figure 5c). The Brillouin shift of the lipid droplets of 8.25 ± 0.02 GHz was also
 354 statistically significantly higher than the Brillouin shift of the surrounding cytoplasm of
 355 7.81 ± 0.02 GHz (Figure 5d). Hence, one could expect that the longitudinal modulus shows
 356 a similar trend as the Brillouin shift as it does for samples described by the two-substance
 357 mixture model. However, the longitudinal modulus of the lipid droplets (2.161 ± 0.005 GPa)

358 was lower than that of the cytoplasm (2.398 ± 0.009 GPa) when the measured RI and ex-
359 tracted absolute density distributions were considered (Figure 5e). The longitudinal mod-
360 ulus of lipid droplets being lower than that of cytoplasm was consistent with previous
361 measurement data of the speed of sound of triacylglycerides which is lower than that
362 of water (Gouw and Vlugter, 1967). In order to demonstrate the effect of the RI and
363 absolute density on the calculation of the longitudinal modulus, we calculated the longi-
364 tudinal modulus under the assumption of a homogeneous RI (1.337) and absolute den-
365 sity (1 g/ml) distribution instead of the values measured, as it would likely be done for a
366 stand-alone Brillouin microscope. The longitudinal modulus of lipid droplets without con-
367 sidering the RI and absolute densities measured results to 2.717 ± 0.022 GPa, which was
368 26% higher than the correctly calculated longitudinal modulus (Figure 5f). Our finding
369 clearly demonstrates that the local distribution of RI and absolute density can contribute
370 considerably to the extraction of the longitudinal modulus of the samples, especially for
371 compartments which cannot be described by the water-based two-substance mixture
372 model.

373 Discussion

374 In this report, we experimentally demonstrated a combined epi-fluorescence, ODT, and
375 Brillouin (FOB) microscopy setup. The colocalized measurements and the subsequent
376 image analysis of the epi-fluorescence intensities and the RI distributions acquired by
377 the FOB setup allowed to identify regions of different material or molecular composi-
378 tion. This enabled us to extract the correct absolute density from either the RI measured
379 by applying the two-substance mixture model, or from the literature in case the two-
380 substance mixture model is not applicable. In combination with the Brillouin shift dis-
381 tributions measured, it was possible to accurately calculate the longitudinal moduli of a
382 specimen. While in principle similar measurements would be possible with two separate
383 setups individually acquiring Brillouin shift and RI, the combined setup simplifies sample
384 handling, eliminates the necessity to locate the same cell or sample region on different
385 setups and substantially reduces the time between the acquisition of the different modal-
386 ties from multiple minutes to a few seconds. The last point is especially important for
387 the analysis of dynamic processes such as the formation of SGs, which otherwise would
388 not be captured adequately. We demonstrated the working principle of the setup using
389 an artificial cell phantom consisting of a PDMS bead embedded in a PAA bead, for which
390 the acquired longitudinal moduli values are consistent with previous studies only when
391 we consider the RI and the absolute density of the PDMS and PAA bead.

392 The setup was also applied to investigate the physical and mechanical properties of
393 intracellular compartments in HeLa cells including nucleoplasm, cytoplasm, and nucleoli.
394 We found that the nucleoplasm has a lower RI and absolute density than the cytoplasm
395 while showing a higher Brillouin shift and longitudinal modulus. We further measured a
396 statistically significantly higher peak linewidth, i.e. viscosity in the nucleoli compared to
397 the other compartments. The nucleus is described as a "network of chromatin and other
398 intranuclear components surrounded by a cytosol fluid" by Wachsmuth *et al.* (2000).
399 This chromatin network was suggested to be responsible for the nucleus' mechanical
400 response in the GHz frequency range as tested with Brillouin microscopy (Zouani *et al.*,
401 2014) and it was shown that the mass density in the cytoskeleton network is higher than
402 in the chromatin network although the Brillouin shift behaves in the opposite way (Liu

403 **et al., 2019).** Hence, it seems reasonable to assume that the chromatin network in the
404 nucleoplasm leads to the higher longitudinal modulus observed in this compartment
405 compared to the cytoplasm, even though the mass density in the nucleoplasm is lower
406 than in the cytoplasm. Further analysis, e.g. testing the response of the longitudinal
407 modulus to chromatin (de)condensation, can be performed to further consolidate this
408 idea. Furthermore, nucleoli, which are formed by liquid-liquid phase separation (LLPS) in
409 the nucleoplasm, and polyQ aggregates, which undergo a rapid liquid-to-solid transition
410 in the cytoplasm, exhibit a statistically significantly higher RI and longitudinal modulus
411 than either nucleoplasm or cytoplasm. However, SGs in P525L HeLa cells, which are also
412 formed by LLPS, did not show statistically significant differences in terms of RI or longi-
413 tudinal modulus compared to the surrounding cytoplasm in living cells, but showed a
414 higher longitudinal modulus compared to the cytoplasm after chemical fixation. Hence,
415 it seems that not every condensation process is accompanied by changes of the RI, ab-
416 solute density or longitudinal modulus. Further investigation is required to reveal the
417 underlying mechanism of how nucleoli consisting of proteins and nucleic acids maintain
418 a higher density and longitudinal modulus than the surrounding nucleoplasm despite
419 the dynamic behavior of compartments formed by LLPS (**Caragine et al., 2019**).

420 Currently, there is a vivid debate whether the Brillouin shift mainly depends on the
421 water content of the specimen, not on its mechanical properties (**Wu et al., 2018c,b; Scar-**
422 **celli and Yun, 2018; Bailey et al., 2019**). If we followed the idea that the water content
423 dominates the Brillouin shift, samples with a higher water content would exhibit a lower
424 Brillouin shift. As the RI of the cytoplasm and the nucleoplasm of the HeLa cells measured
425 here is linearly proportional to the mass density of macromolecules in water solution
426 (**Barer, 1952; Popescu et al., 2008**) and the refraction increments of both compartments
427 are similar (**Zhao et al., 2011; Zangle and Teitell, 2014**), the lower RI of the nucleoplasm
428 compared to the cytoplasm indicates that the nucleoplasm has a higher water content
429 than the cytoplasm. However, the nucleoplasm exhibits a higher Brillouin shift and lon-
430 gitudinal modulus than the surrounding cytoplasm. Hence, this result indicates that the
431 Brillouin shift and the longitudinal modulus are not only governed by the water content,
432 but are at least substantially influenced by the mechanical properties of the specimen.

433 An important aspect of the calculation of the longitudinal moduli is the extraction of
434 the densities of the samples. For samples or compartments that can be described by the
435 two-substance mixture model, we exploited the linear relation between the RI and the
436 mass density to calculate the absolute density value (**Barer, 1952; Popescu et al., 2008;**
437 **Zangle and Teitell, 2014**). However, as the partial specific volume of the dry fraction
438 is unknown, this approach might overestimate the absolute density by approximately
439 10 % (see Methods). We find that in all samples measured here where the two-substance
440 mixture model can be applied, neglecting the contribution of RI and density to the longi-
441 tudinal modulus still yields a similar tendency for the longitudinal modulus and Brillouin
442 shift (i.e. a high Brillouin shift means a high longitudinal modulus and vice versa), but
443 doing so might lead to a systematic error for the longitudinal modulus. For cell com-
444 parts mainly containing a single substance, where this model cannot be applied,
445 e.g. lipid droplets in adipocytes, we used the specificity provided by the epi-fluorescence
446 imaging to identify the respective regions and employed the literature value for the ab-
447 solute density in this region. Using this approach, we found that although the RI and Bril-
448 louin shift of the lipid compartments in adipocytes are higher than those values of the

449 cytoplasm, the resulting longitudinal modulus is actually lower when taking into account
450 the RI and absolute density distribution. This illustrates that RI and absolute density do
451 not cancel out for every cell and compartment – an implicit assumption in many studies
452 acquiring only the Brillouin shift – and that RI and absolute density have to be known in
453 order to precisely calculate the longitudinal modulus.

454 However, both the calculation of the absolute density from the RI and the identifica-
455 tion of regions not described by the two-substance mixture model rely on the knowledge
456 of the molecular composition of the sample. In order to calculate the absolute density
457 from the RI, the refraction increment has to be known, which, albeit comparable for pro-
458 teins and nucleic acids, might slightly vary between different cell compartments depend-
459 ing on their composition. Obviously, the composition also plays an important role when
460 selecting the correct literature value for the absolute density of compartments where
461 the two-substance mixture model is not applicable. As the molecular composition can-
462 not be resolved exactly by the FOB microscope, we used the refraction increment or
463 absolute density of the constituent likely predominant in a certain compartment. This
464 might lead to a slight deviation of the absolute density from the exact value, e.g. in the
465 membrane-rich perinuclear region of HeLa cells where the absolute density might be
466 underestimated. To overcome this issue and use the appropriate refraction increment
467 or absolute density for a mixture of different proteins, nucleic acids, or phospholipids,
468 more sophisticated labeling and staining of different molecules and the use of several
469 fluorescence channels might allow identifying multiple substances. Also, the absolute
470 concentration of different molecules could be directly measured from the intensity of
471 Raman scattering signals (*Oh et al., 2019*), an imaging extension that could be added for
472 future studies to the FOB setup presented here (*Traverso et al., 2015; Mattana et al.,*
473 *2018*).

474 Further improvements of the setup could include moving to a laser source with a
475 wavelength of 660 nm or longer to reduce cell damage due to phototoxicity (*Nikolić and*
476 *Scarcelli, 2019*). This would allow a higher laser power at the sample plane for Brillouin
477 microscopy, which reduces the acquisition time and could help analysing dynamic pro-
478 cesses. To correlate the RI value and Brillouin frequency shift of the samples at the same
479 wavelength, the FOB setup uses the same laser source for ODT and Brillouin mode. Bril-
480 louin spectroscopy requires a laser with an extremely narrow linewidth that, hence, has
481 a high temporal coherence length. While the coherent nature of the laser illumination
482 makes ODT susceptible to speckle noise, the ODT system used achieves a RI uncertainty
483 of 4.15×10^{-5} (which corresponds to a difference in protein concentration of 0.22 mg/ml)
484 (*Kim and Guck, 2020*) that is sufficient to pick up the RI differences between the various
485 regions of the cells characterized here. The speckle noise could be further reduced by
486 using a dynamic diffuser (*Choi et al., 2011*) or numerical filtering approaches (*Bianco*
487 *et al., 2018*). Furthermore, the setup could be enhanced to measure not only longitudi-
488 nal phonons, but also transverse phonons, which are related to the shear modulus and
489 can generally not propagate in liquids. Hence, this could help to discriminate liquid-like
490 versus solid-like materials (*Kim et al., 2016b; Prevedel et al., 2019*). The limitation of op-
491 tical diffraction tomography to weakly scattering samples like single cells or beads could
492 be overcome by the implementation of tomogram reconstruction algorithms taking into
493 account multiple light scattering in the sample (*Lim et al., 2019; Chowdhury et al., 2019*).
494 This would enable the setup to measure tissues and organisms.

495 Although Brillouin microscopy was introduced to biology more than a decade ago
496 (*Scarcelli and Yun, 2008*), its relevance to biological questions is sometimes still viewed
497 skeptically in the field of mechanobiology. This is mainly due to the fact that the main
498 quantity measured – the longitudinal modulus – relates to the rarely acquired compress-
499 ibility in a frequency range to which cells might not be sensitive. However, multiple stud-
500 ies observed changes of the longitudinal modulus due to biophysical processes. The
501 modulus changes due to the inhibition of actin polymerization (*Scarcelli et al., 2015; An-*
502 *tonacci and Braakman, 2016*) and after spinal cord injury (*Schlüßler et al., 2018*), after
503 UV-induced polymer crosslinking (*Scarcelli and Yun, 2008*) or actin polymerization into a
504 gel (*Scarcelli et al., 2015*). For various samples, e.g. cells under osmotic shock, bovine
505 lenses or zebrafish tissue, phenomenological correlations with the Young's modulus have
506 been found (*Scarcelli and Yun, 2011; Scarcelli et al., 2015; Schlüßler et al., 2018*), implying
507 that for these tissues the two moduli could serve as a proxy for each other. Furthermore,
508 Brillouin microscopy gives access to other quantities besides the compressibility. The
509 viscosity and shear modulus of a sample are also accessible by Brillouin microscopy by
510 evaluating the peak linewidth and observing transverse phonons (*Antonacci et al., 2018;*
511 *Kim et al., 2016b; Prevedel et al., 2019*) and can be influenced e.g. by liquid-to-solid phase
512 transitions. For the observed, physically real variations of the longitudinal modulus and
513 viscosity to affect biophysical processes, it is moreover not necessary that cells or organ-
514 isms are able to sense these mechanical differences directly in the first place, as would
515 be relevant in the context of mechanosensing. It seems entirely possible that the varia-
516 tions in the longitudinal modulus at GHz frequencies detected in cells will turn out to be
517 reporting on local changes in intermolecular interactions, water mobility and hydration
518 shells, and other aspects relevant for emergent, supramolecular processes, which are
519 important in their own right. We thus believe that Brillouin microscopy can contribute
520 to open questions in biology, but further studies are necessary to finally establish its
521 relevance.

522 In conclusion, the FOB setup allows a precise calculation of the longitudinal modulus
523 from the measured RI and Brillouin shift even for samples with a heterogeneous RI and
524 absolute density distribution. This enables quantitative measurements of the mechani-
525 cal properties of single cells and their compartments and might potentially contribute to
526 a better understanding of physiological and pathological processes such as phase sepa-
527 ration and transition in cells as a response to external stress.

528 Methods

529 Optical setup

530 The FOB microscope setup combines optical diffraction tomography (ODT), Brillouin mi-
531 croscopy and epi-fluorescence imaging in the same optical system. It allows to obtain
532 quantitative maps of the refractive indices (RI), the Brillouin shifts, and the fluorescence
533 and brightfield intensities of a sample.

534 In order to acquire the three-dimensional RI distribution, ODT employing Mach-Zehn-
535 der interferometry is applied. Besides small modifications necessary for the combination
536 with Brillouin microscopy the ODT part of the setup is identical to the one presented in
537 *Abuhattum et al. (2018)*. As laser source a frequency-doubled Nd-YAG laser (Torus 532,
538 Laser Quantum Ltd, United Kingdom) with a wavelength of 532 nm and a maximum output

539 power of 750 mW is used for both ODT and Brillouin microscopy. The laser was chosen as
540 it offers a very low amplified spontaneous emission intensity of 110 dB necessary for Brillouin
541 measurements. The main beam of the laser is coupled into a single-mode fiber and
542 split into two beams by a 2 x 2 fiber coupler. One beam is used as the reference for the
543 Mach-Zehnder interferometer. The other beam is collimated and demagnified through a
544 tube lens with a focal length of 175 mm and a 40x/1.0 NA water dipping objective lens (Carl
545 Zeiss AG, Germany), and illuminates the sample in a custom-built inverted microscope.
546 To allow to reconstruct a three-dimensional RI tomogram of the sample, the sample is
547 illuminated under 150 different incident angles. The illumination angles are generated
548 by a dual-axis galvanometer mirror (GVS012/M, Thorlabs Inc., USA) which is placed at the
549 conjugate plane of the sample and diffracts the illumination beam. The diffracted beam
550 is collected by a 63x/1.2 NA water immersion objective lens (Carl Zeiss AG, Germany) and
551 a tube lens with a focal length of 200 mm. The sample and the reference beam then interfere
552 at the image plane of a CCD camera (FL3-U3-13Y3M-C, FLIR Systems Inc., USA) which
553 records the generated spatially modulated hologram of the sample. In some cases the
554 hologram additionally shows parasitic interference patterns originating from the protective
555 window in front of the CCD camera (see e.g. Figure 2b. This is a general limitation
556 of the ODT setup, due to the coherent nature of the laser source). The setup achieves a
557 spatial resolution of 0.25 μm within the lateral plane and 0.5 μm in the axial direction.

558 In order to switch to Brillouin microscopy mode, a motorized mirror is moved into
559 the beam path guiding the light towards an additional lens with a focal length of 300 mm.
560 In combination with the upper tube lens this ensures a collimated beam before the mi-
561 croscope objective and effectively creates a laser focus at the sample plane. Hence, in
562 Brillouin mode the galvanometer mirrors are located at the Fourier conjugate plane of
563 the sample and can move the laser focus in the sample plane (Figure 1a, inset). This al-
564 lows to scan the laser focus over the sample by adjusting the galvanometer voltage. The
565 relation between the applied galvanometer voltage and the resulting focus position is cal-
566 briated by acquiring images of the laser foci with the ODT camera and extracting the foci
567 positions for different galvanometer voltages. The Brillouin scattered light is collected in
568 the backscattering configuration with the same objective used for ODT and coupled into
569 a single-mode fiber which acts as a pinhole confocal to the illumination fiber and deliv-
570 ers the light to a two-stage virtually imaged phased array (VIPA) Brillouin spectrometer
571 (*Scarcelli and Yun, 2011; Scarcelli et al., 2015*). This results in a spatial resolution of 0.4 μm
572 within the lateral plane and approximately 1 μm in the axial direction. In the spectrome-
573 ter the beam is collimated and passes through the iodine absorption cell, which blocks
574 the Rayleigh scattered and reflected light. The beam is then guided to two VIPA inter-
575 ferometers (OP-6721-3371-2, Light Machinery, Canada) with 30 GHz free spectral range
576 and a spectral resolution of approximately $\delta\nu = 350$ MHz, which is comparable to values
577 reported for other VIPA based setups (*Antonacci et al., 2013*) but lower than the spec-
578 tral resolution achievable with stimulated Brillouin scattering setups of around 100 MHz
579 (*Remer et al., 2020*). The Brillouin spectrum is imaged with an sCMOS camera (Neo 5.5,
580 Andor, USA) with a typical exposure time of 0.5 s at a laser power of 10 mW at the sample.

581 Furthermore, the laser frequency is stabilized to the absorption maximum of a trans-
582 sition line of molecular iodine by controlling the laser cavity temperature. This allows to
583 attenuate the intensity of the Rayleigh scattered light entering the Brillouin spectrometer,
584 eliminates potential laser frequency drifts (*Meng et al., 2014; Schlüßler et al., 2018*) and

585 simplifies the mechanical alignment of the spectrometer as no masks for blocking the
586 elastically scattered light are necessary. To generate an error signal for the frequency
587 stabilization loop a small fraction of the laser light is frequency shifted by 350 MHz by
588 an acousto-optic modulator (AOM 3350-125, EQ Photonics GmbH, Germany) and guided
589 through an absorption cell (TG-ABI-Q, Precision Glass Blowing, USA) filled with iodine I_2 .
590 The beam intensity is measured before and after the absorption cell by two photodetec-
591 tors (PDA36A2, Thorlabs Inc., USA) and a data acquisition card (PicoScope 2205A, Pico
592 Technology, United Kingdom). The quotient of both intensities is a measure for the ab-
593 sorption due to the iodine vapor. The laser cavity temperature is then controlled with
594 a custom C++ software LQTControl to achieve an absorption of 50 % for the frequency
595 shifted stabilization beam, which leads to maximum absorption for the not shifted main
596 beam.

597 To realise epi-fluorescence imaging, an incoherent beam from a white light halogen
598 lamp (DC-950, Dolan-Jenner Industries Inc., USA) is coupled into the setup by a three-
599 channel dichroic mirror (FF409/493/596-Di01-25x36, Semrock, USA). The bandwidth of
600 the excitation and emission beam is selected by two motorized filter sliders equipped
601 with band-pass filters in front of the halogen lamp and the CCD camera. A white light LED
602 (Thorlabs, USA) coupled into the Brillouin illumination path allows to observe a brightfield
603 image of the sample during Brillouin acquisition. Since fluorescence imaging and ODT
604 use the same objective, the acquired fluorescence images are guaranteed to focus the
605 central plane of the acquired RI tomogram.

606 The two cameras and all moveable optical devices of the setup are controlled with
607 a custom acquisition program written in C++. The software allows to control all three
608 imaging modalities and stores the acquired data as an HDF5 file.

609 **Refractive index tomogram reconstruction**

610 From the spatially modulated holograms recorded, the complex optical field of the light
611 scattered by the sample is retrieved by a field retrieval algorithm based on the Fourier
612 transform (*Cuche et al., 2000*). The RI tomogram of the sample is reconstructed from
613 the retrieved optical fields with various incident angles via the Fourier diffraction the-
614 rem. The detailed procedure for the tomogram reconstruction is presented in *Kim et al.*
615 (*2014*); *Müller et al. (2016)*. The field retrieval and tomogram reconstruction were per-
616 formed by custom-made MATLAB (The MathWorks, Natick, USA) scripts. From the recon-
617 structed RI tomograms, subcellular compartments are segmented based on the RI and
618 epi-fluorescence signals. First, cell regions are segmented from background by apply-
619 ing the Otsu's thresholding method, and the watershed algorithm is used to determine
620 individual cells in the RI tomograms. Then, epi-fluorescence images of the fluorescence-
621 labeled subcellular compartments (e.g., nuclei, polyQ aggregates in HeLa cells, nuclei
622 and lipid droplets in adipocytes) are colocalized with the RI tomograms to segment the
623 compartments. In the nuclei of the HeLa cells, the RI tomogram regions having higher RI
624 values than surrounding nucleoplasm are segmented by the Otsu's thresholding method
625 and identified as nucleoli. The detailed segmentation procedure is described elsewhere
626 (*Schürmann et al., 2016; Kim and Guck, 2020*), and the source code for the segmentation
627 can be found at <https://github.com/OpticalDiffractionTomography/NucleiAnalysis>.

628 Brillouin shift evaluation

629 To evaluate the Brillouin shift v_B , a custom MATLAB program is used. Details of the eval-
630 uation process can be found in *Schlüßler et al. (2018)*.

631 Calculation of the longitudinal modulus

632 The longitudinal modulus M' is determined by

$$633 M' = \rho \left(\frac{\lambda v_B}{2n \cos(\Theta/2)} \right)^2 \quad (1)$$

633 where the wavelength λ of the laser source and the scattering angle Θ are known parame-
634 ters of the setup. The RI n and the Brillouin shift v_B of the sample are measured using the
635 FOB microscope. The absolute density ρ can be calculated for the majority of biological
636 samples from the RI assuming a two-substance mixture. The absolute density is given
637 by (*Barer, 1952; Davies and Wilkins, 1952; Zangle and Teitell, 2014; Popescu et al., 2008;*
638 *Schlüßler et al., 2018*)

$$639 \rho = \frac{n - n_{\text{fluid}}}{\alpha} + \rho_{\text{fluid}} \cdot (1 - \rho_{\text{dry}} \cdot \bar{v}_{\text{dry}}). \quad (2)$$

639 with the RI n_{fluid} of the medium, the refraction increment α ($\alpha = 0.190 \text{ mL/g}$ for proteins
640 and nucleic acid (*Zhao et al., 2011; Zangle and Teitell, 2014; Biswas et al., 2021*)), the
641 absolute density ρ_{fluid} of the medium, the absolute density ρ_{dry} and the partial specific
642 volume \bar{v}_{dry} of the dry fraction. In case of $\rho_{\text{dry}} \ll \frac{1}{\bar{v}_{\text{dry}}}$ this can be simplified to

$$643 \rho \approx \frac{n - n_{\text{fluid}}}{\alpha} + \rho_{\text{fluid}}. \quad (3)$$

643 This simplification leads to an overestimation of the absolute density and, hence, the lon-
644 gitudinal modulus, of around 10 % for e.g. HeLa cells, which we believe to be acceptable.

645 For certain cell types, e.g. adipocyte cells, the two-substance mixture model cannot be
646 applied for all cell compartments, i.e. the lipid droplets inside these cells do only consist
647 of lipids. Applying the two-substance model here leads to an unphysiological overesti-
648 mation of the absolute density. Hence, in special cases the absolute density cannot be
649 inferred from the RI and has to be estimated from the literature. This is possible with the
650 FOB microscope, since fluorescence labeling of the lipid droplets allows to identify cell
651 regions governed by e.g. lipids.

652 In order to calculate the longitudinal modulus and visualize the measurement results
653 of the FOB microscope, a custom MATLAB program FOBVisualizer is used. The software
654 allows to adjust the spatial alignment of the Brillouin and ODT measurements by cross-
655 correlating the two-dimensional maps acquired by both modalities and shifting the Bril-
656 loun maps towards the highest correlation coefficient.

657 Statistical analysis

658 For the statistical analysis of the RI and longitudinal modulus differences between cyto-
659 plasm, nucleoplasm and nucleoli (Figure 2, Figure 3 and Figure 4) the Kruskal-Wallis test in
660 combination with a least significant difference post-hoc test was used. The shown aster-
661 isks indicate the significance levels: $*p < 0.05$, $**p < 0.01$, $***p < 0.001$ and $****p < 0.0001$.
662 In box-and-whisker plots, the center lines indicate the medians, the edges of the boxes
663 define the 25th and 75th percentiles, the red plus signs represent data points outside the
664 $\pm 2.7\sigma$ range which are considered outliers and the whiskers extend to the most extreme
665 data value that is not an outlier.

666 Cell phantom preparation

667 Artificial cell phantoms, consisting of polydimethylsiloxane (PDMS, Dow Corning Sylgard®
668 184) particles embedded in larger polyacrylamide microgel beads, were produced as fol-
669 low. The PDMS particles were generated by vortex-mixing a solution of 1 g PDMS (10:1
670 w/w, base/curing agent) dispersed in 10 ml of 2 % w/v poly(ethylene glycol) monooleate
671 (Merck Chemicals GmbH, Germany) aqueous solution. After mixing, the emulsion was
672 kept overnight in an oven at 75 °C to allow the polymerization of the PDMS droplets. The
673 size dispersion of the PDMS particle was reduced by centrifugation and removing all par-
674 ticles with a diameter larger than 5 µm. The final solution, containing PDMS particles with
675 a diameter lower than 5 µm, was washed three times in Tris-buffer (pH 7.48) and resus-
676 pended in 1 % w/v Pluronic® F-127 (Merck Chemicals GmbH, Germany) Tris-Buffer.

677 1 µl of concentrated PDMS particles were added to 100 µl polyacrylamide pre-gel mix-
678 ture with a total monomer concentration of 11.8 % w/v. This solution was used as a dis-
679 persed phase in a flow-focusing microfluidic device to produce PAAm microgel beads,
680 as previously described in *Girardo et al. (2018)*, embedding PDMS particles. N-hydroxy-
681 succinimide ester (0.1 % w/v, Merck Chemicals GmbH, Germany) was added to the oil
682 solution to functionalize the phantoms with Alexa 488. Precisely, 100 µl of Alexa Fluor™ hy-
683 drazide 488 (ThermoFisher Scientific, Germany) in deionized water (1 mg/ml) was added
684 to 100 µl phantom pellet and incubated overnight at 4 °C. The unbonded fluorophores
685 were removed by three washings in PBS. The final functionalized phantoms were stored
686 in PBS at 4 °C.

687 Cell preparation

688 The stable HeLa cell line expressing GFP fused to the N terminus of NIFK (Nucleolar pro-
689 tein interacting with the FHA domain of MKI67), was kindly provided by the lab of Anthony
690 Hyman (Max Planck Institute of Molecular Cell Biology and Genetics). The cells were cul-
691 tured in Dulbecco's modified Eagle's medium (DMEM) (31966-021, Thermo Fisher), high
692 glucose with GlutaMax medium (61965-026, Gibco) under standard conditions at 37 °C
693 and 5 % CO₂. The culture medium was supplemented with 10 % fetal bovine serum (FBS)
694 and 1 % penicillin-streptomycin. The cells were subcultured in a glass-bottom Petri dish
695 (FluoroDish, World Precision Instruments Germany GmbH) one day prior to the measure-
696 ment, and the culture medium was exchanged to Leibovitz's L-15 Medium without phenol
697 red (21083027, Thermo Fisher Scientific) prior to imaging. For staining nuclei, the cells
698 were stained with Hoechst (1:1000 dilution) for 10 min and washed with fresh Leibovitz's
699 L-15 medium prior to imaging.

700 The wild-type HeLa cells transiently expressing amyloid (Q103-GFP) aggregates were
701 cultured in DMEM (31966-021, Thermo Fisher), high glucose with GlutaMax medium (61965-
702 026, Gibco) under standard conditions at 37 °C and 5 % CO₂. The culture medium was
703 supplemented with 10 % fetal bovine serum (FBS) and 1 % penicillin-streptomycin. The
704 cells were subcultured in a glass-bottom Petri dish (FluoroDish, World Precision Instru-
705 ments Germany GmbH) two days prior to the measurement. One day prior to the mea-
706 surement the cells were transiently transfected with pcDNA3.1-Q103-GFP using Lipo-
707 fectamine 2000 (Invitrogen, Carlsbad, California). Directly before the imaging the cul-
708 ture medium was exchanged to Leibovitz's L-15 Medium without phenol red (21083027,
709 Thermo Fisher Scientific).

710 The HeLa cells FUS-GFP WT (wild-type) and FUS-GFP^{P525L} (disease model for amy-

711 otrophic lateral sclerosis) were kindly provided by the lab of Anthony Hyman (Max Planck
712 Institute of Molecular Cell Biology and Genetics). The cells were cultured in 89 % DMEM
713 supplemented with 10 % FBS (Sigma-Aldrich; F7524) and 1 % penicillin-streptomycin under
714 standard conditions at 37 °C and 5 % CO₂. One day before the experiment the cells were
715 transferred to a 35 mm glass-bottom Petri dish (FluoroDish, World Precision Instruments
716 Germany GmbH). 30 min prior to the measurements the culture medium was exchanged
717 to Leibovitz's L-15 medium without phenol red (21083027, Thermo Fisher Scientific) and
718 the non-control samples were treated with 5 mM sodium arsenite. For fixation the ar-
719 senite treated cells were washed with PBS, fixed with 4 % paraformaldehyde for 10 min at
720 room temperature, washed with PBS twice and left in PBS for FOB microscopy measure-
721 ments.

722 **Adipocyte preparation**

723 Simpson-Golabi-Behmel Syndrome (SGBS) preadipocytes were cultured and differenti-
724 ated as described previously (*Wabitsch et al., 2001; Fischer-Pozovszky et al., 2008*). For
725 regular cell culture, cells were maintained in Dulbecco's modified Eagles' Medium (DMEM)
726 / nutrient F-12 Ham (Thermofisher) supplemented with 4 µM pantothenic, 8 µM biotin
727 (Pan/Bio), 100 U/ml penicillin/100 µg/ml streptomycin (=OF-medium) with 10 % FBS (OF-
728 medium +FBS, Thermofisher) at 37 °C in T75 flasks. For adipogenic differentiation, cells
729 were washed with PBS, detached using TrypLE Express (Thermofisher) and seeded onto
730 glass-bottom Petri dishes (FluoroDish, World Precision Instruments Germany GmbH, 35 mm,
731 10⁵ cells). After 24 hours, cells were washed three times with serum-free OF-Medium,
732 and differentiation medium was added, consisting of OF-medium complemented with
733 10 µg/ml human transferrin (Sigma-Aldrich), 20 nM human insulin (Sigma-Aldrich), 2 µM
734 rosiglitazone (Cayman), 100 nM desxamethasone (Sigma-Aldrich), 250 µM 3-isobutyl-1-me-
735 thylxantine IBMX (Sigma-Aldrich), 100 nM cortisol (Sigma-Aldrich) and 0.2 nM triiodothyro-
736 nine T3 (Sigma-Aldrich). On day 4, the medium was exchanged to OF-medium supple-
737 mented with only transferrin, insulin, cortisol, T3 (concentrations as above). The medium
738 was replaced every fourth day. Cells were probed on day 11 of adipogenic differentiation.

739 **Cell lines**

740 HeLa WT cells were a kind gift of F. Buchholz (Technische Universität Dresden, Germany).
741 The HeLa cell line transfected with GFP:NIFK, HeLa WT FUS-GFP and HeLa P525L FUS-GFP
742 were a kind gift of A. Hyman (Max Planck Institute of Molecular Cell Biology and Genetics,
743 Dresden, Germany). Simpson-Golabi-Behmel Syndrome (SGBS) adipocytes were a kind
744 gift of Prof. Martin Wabitsch (Centre for Hormonal Disorders in Children and Adolescents
745 – Ulm University Hospital).

746 No authentication was performed. All cell lines tested negative for mycoplasma con-
747 tamination. No commonly misidentified cell lines were used.

748 **Code availability**

749 The source code of LQTControl, the program to stabilize the laser cavity temperature, is
750 open source and can be found on GitHub (<https://github.com/BrillouinMicroscopy/LQTControl>). The same is true for BrillouinAcquisition, the program for controlling and data
751 acquisition of the FOB microscope (<https://github.com/BrillouinMicroscopy/BrillouinAcquisition>), BrillouinEvaluation, used for evaluating Brillouin data (<https://github.com/BrillouinEvaluation>).

754 [IouinMicroscopy/BrillouinEvaluation](#)) and FOBVisualizer, used for viewing FOB microscopy
755 data (<https://github.com/BrillouinMicroscopy/FOBVisualizer>). The Matlab scripts for
756 cell segmentation and ODT reconstruction can be found under <https://github.com/OpticalDiffractionTomography/NucleiAnalysis> and https://github.com/OpticalDiffractionTomography/ODT_Reconstruction, respectively.
758

759 **Data availability**

760 The data sets generated during and/or analyzed during the current study are available
761 from figshare under the following link: <https://doi.org/10.6084/m9.figshare.c.5347778>.

762 References

763 **Abuhattum S**, Kim K, Franzmann TM, Eßlinger A, Midtvedt D, Schlüßler R, Möllmert S, Kuan HS,
764 Alberti S, Zaburdaev V, Guck J. Intracellular Mass Density Increase Is Accompanying but Not
765 Sufficient for Stiffening and Growth Arrest of Yeast Cells. *Frontiers in Physics*. 2018; 6. doi:
766 [10.3389/fphy.2018.00131](https://doi.org/10.3389/fphy.2018.00131).

767 **Alberti S**, Dormann D. Liquid–Liquid Phase Separation in Disease. *Annual Review of Genetics*.
768 2019; 53(1):171–194. doi: 10.1146/annurev-genet-112618-043527.

769 **Alberti S**, Hyman AA. Are Aberrant Phase Transitions a Driver of Cellular Aging? *BioEssays: News
770 and Reviews in Molecular, Cellular and Developmental Biology*. 2016 Oct; 38(10):959–968. doi:
771 [10.1002/bies.201600042](https://doi.org/10.1002/bies.201600042).

772 **Antonacci G**, Beck T, Bilenca A, Czarske J, Elsayad K, Guck J, Kim K, Krug B, Palombo F, Prevedel
773 R, Scarcelli G. Recent Progress and Current Opinions in Brillouin Microscopy for Life Science
774 Applications. *Biophysical Reviews*. 2020 Jun; 12(3):615–624. doi: 10.1007/s12551-020-00701-9.

775 **Antonacci G**, Braakman S. Biomechanics of Subcellular Structures by Non-Invasive Brillouin Mi-
776 croscopy. *Scientific Reports*. 2016 Nov; 6(1):37217. doi: 10.1038/srep37217.

777 **Antonacci G**, de Turris V, Rosa A, Ruocco G. Background-Deflection Brillouin Microscopy Reveals
778 Altered Biomechanics of Intracellular Stress Granules by ALS Protein FUS. *Communications Bi-
779 ology*. 2018 Dec; 1(1):139. doi: 10.1038/s42003-018-0148-x.

780 **Antonacci G**, Foreman MR, Paterson C, Török P. Spectral Broadening in Brillouin Imaging. *Applied
781 Physics Letters*. 2013 Nov; 103(22):221105. doi: [10.1063/1.4836477](https://doi.org/10.1063/1.4836477).

782 **Bailey M**, Alunni-Cardinali M, Correa N, Caponi S, Holsgrove T, Barr H, Stone N, Winlove CP,
783 Fioretto D, Palombo F. Brillouin-Derived Viscoelastic Parameters of Hydrogel Tissue Models.
784 arXiv:191208292 [cond-mat, physics:physics]. 2019 Dec; .

785 **Bambadekar K**, Clément R, Blanc O, Chardès C, Lenne PF. Direct Laser Manipulation Reveals the
786 Mechanics of Cell Contacts in Vivo. *Proceedings of the National Academy of Sciences*. 2015 Feb;
787 112(5):1416–1421. doi: [10.1073/pnas.1418732112](https://doi.org/10.1073/pnas.1418732112).

788 **Barer R**. Interference Microscopy and Mass Determination. *Nature*. 1952 Mar; 169(4296):366–367.
789 doi: 10.1038/169366b0.

790 **Bäuerlein FJB**, Saha I, Mishra A, Kalemanov M, Martínez-Sánchez A, Klein R, Dudanova I, Hipp MS,
791 Hartl FU, Baumeister W, Fernández-Busnadio R. In Situ Architecture and Cellular Interactions
792 of PolyQ Inclusions. *Cell*. 2017 Sep; 171(1):179–187.e10. doi: [10.1016/j.cell.2017.08.009](https://doi.org/10.1016/j.cell.2017.08.009).

793 **Bianco V**, Memmolo P, Leo M, Montresor S, Distante C, Paturzo M, Picart P, Javidi B, Ferraro P.
794 Strategies for Reducing Speckle Noise in Digital Holography. *Light: Science & Applications*. 2018
795 Aug; 7(1):48. doi: 10.1038/s41377-018-0050-9.

796 **Biswas A**, Kim K, Cojoc G, Guck J, Reber S. The Xenopus Spindle Is as Dense as the Surrounding
797 Cytoplasm. *Developmental Cell*. 2021; .

798 **Boyd RW**. *Nonlinear Optics*. Academic Press; 2008.

799 **Braet F**, Rotsch C, Wisse E, Radmacher M. Comparison of Fixed and Living Liver Endothe-
800 lial Cells by Atomic Force Microscopy. *Applied Physics A*. 1998 Mar; 66(1):S575–S578. doi:
801 10.1007/s003390051204.

802 **Brangwynne CP**, Eckmann CR, Courson DS, Rybarska A, Hoege C, Gharakhani J, Jülicher F,
803 Hyman AA. Germline P Granules Are Liquid Droplets That Localize by Controlled Dissolu-
804 tion/Condensation. *Science*. 2009 Jun; 324(5935):1729–1732. doi: [10.1126/science.1172046](https://doi.org/10.1126/science.1172046).

805 **Brangwynne CP**, Mitchison TJ, Hyman AA. Active Liquid-like Behavior of Nucleoli Determines Their
806 Size and Shape in *Xenopus Laevis* Oocytes. *Proceedings of the National Academy of Sciences*.
807 2011 Mar; 108(11):4334–4339. doi: [10.1073/pnas.1017150108](https://doi.org/10.1073/pnas.1017150108).

808 **Brillouin L.** Diffusion de La Lumière et Des Rayons X Par Un Corps Transparent Homogène
809 - Influence de l'agitation Thermique. *Ann Phys.* 1922; 9(17):88–122. doi: [10.1051/annphys/192209170088](https://doi.org/10.1051/annphys/192209170088).

811 **Cafarelli A**, Verbeni A, Poliziani A, Dario P, Menciassi A, Ricotti L. Tuning Acoustic and Mechanical
812 Properties of Materials for Ultrasound Phantoms and Smart Substrates for Cell Cultures. *Acta
813 Biomaterialia*. 2017 Feb; 49:368–378. doi: [10.1016/j.actbio.2016.11.049](https://doi.org/10.1016/j.actbio.2016.11.049).

814 **Caragine CM**, Haley SC, Zidovska A. Nucleolar Dynamics and Interactions with Nucleoplasm in
815 Living Cells. *eLife*. 2019 Nov; 8:e47533. doi: [10.7554/eLife.47533](https://doi.org/10.7554/eLife.47533).

816 **Choi Y**, Yang TD, Lee KJ, Choi W. Full-Field and Single-Shot Quantitative Phase Microscopy
817 Using Dynamic Speckle Illumination. *Optics Letters*. 2011 Jul; 36(13):2465–2467. doi:
818 [10.1364/OL.36.002465](https://doi.org/10.1364/OL.36.002465).

819 **Chowdhury S**, Chen M, Eckert R, Ren D, Wu F, Repina N, Waller L. High-Resolution 3D Refrac-
820 tive Index Microscopy of Multiple-Scattering Samples from Intensity Images. *Optica*. 2019 Sep;
821 6(9):1211–1219. doi: [10.1364/OPTICA.6.001211](https://doi.org/10.1364/OPTICA.6.001211).

822 **Christ AF**, Franze K, Gautier H, Moshayedi P, Fawcett J, Franklin RJM, Karadottir RT, Guck J.
823 Mechanical Difference between White and Gray Matter in the Rat Cerebellum Measured
824 by Scanning Force Microscopy. *Journal of Biomechanics*. 2010; 43(15):2986–2992. doi:
825 <http://dx.doi.org/10.1016/j.jbiomech.2010.07.002>.

826 **Cotte Y**, Toy F, Jourdain P, Pavillon N, Boss D, Magistretti P, Marquet P, Depeursinge C. Marker-Free
827 Phase Nanoscopy. *Nature Photonics*. 2013 Feb; 7(2):113–117. doi: [10.1038/nphoton.2012.329](https://doi.org/10.1038/nphoton.2012.329).

828 **Cuche E**, Marquet P, Depeursinge C. Spatial Filtering for Zero-Order and Twin-Image Elim-
829 ination in Digital off-Axis Holography. *Applied Optics*. 2000 Aug; 39(23):4070–4075. doi:
830 [10.1364/ao.39.004070](https://doi.org/10.1364/ao.39.004070).

831 **Davies HG**, Wilkins MHF. Interference Microscopy and Mass Determination. *Nature*. 1952 Mar;
832 169(4300):541–541. doi: [10.1038/169541a0](https://doi.org/10.1038/169541a0).

833 **Engler AJ**, Sen S, Sweeney HL, Discher DE. Matrix Elasticity Directs Stem Cell Lineage Specification.
834 *Cell*. 2006 Aug; 126(4):677–689. doi: [10.1016/j.cell.2006.06.044](https://doi.org/10.1016/j.cell.2006.06.044).

835 **Erbe A**, Sigel R. Tilt Angle of Lipid Acyl Chains in Unilamellar Vesicles Determined by Ellipsometric
836 Light Scattering. *The European Physical Journal E, Soft Matter*. 2007 Apr; 22(4):303–309. doi:
837 [10.1140/epje/e2007-00038-5](https://doi.org/10.1140/epje/e2007-00038-5).

838 **Fiore A**. Direct Three-Dimensional Measurement of Refractive Index via Dual Photon-Phonon Scat-
839 tering. *Physical Review Letters*. 2019; 122(10). doi: [10.1103/PhysRevLett.122.103901](https://doi.org/10.1103/PhysRevLett.122.103901).

840 **Fischer-Posovszky P**, Newell FS, Wabitsch M, Tornqvist HE. Human SGBS Cells - a Unique Tool for
841 Studies of Human Fat Cell Biology. *Obesity Facts*. 2008; 1(4):184–189. doi: [10.1159/000145784](https://doi.org/10.1159/000145784).

842 **Franze K**, Janmey PA, Guck J. Mechanics in Neuronal Development and Repair. *Annual Review of
843 Biomedical Engineering*. 2013; 15(1):227–251. doi: [10.1146/annurev-bioeng-071811-150045](https://doi.org/10.1146/annurev-bioeng-071811-150045).

844 **Gautier HOB**, Thompson AJ, Achouri S, Koser DE, Holtzmann K, Moeendarbary E, Franze K. Atomic
845 Force Microscopy-Based Force Measurements on Animal Cells and Tissues. In: *Methods in Cell*
846 *Biology*, vol. 125 Elsevier; 2015.p. 211–235. doi: [10.1016/bs.mcb.2014.10.005](https://doi.org/10.1016/bs.mcb.2014.10.005).

847 **Girardo S**, Träber N, Wagner K, Cojoc G, Herold C, Goswami R, Schlüßler R, Abuhattum S, Tauben-
848 berger A, Reichel F, Mokbel D, Herbig M, Schürmann M, Müller P, Heida T, Jacobi A, Ulbricht E,
849 Thiele J, Werner C, Guck J. Standardized Microgel Beads as Elastic Cell Mechanical Probes. *Journal*
850 *of Materials Chemistry B*. 2018 Sep; doi: [10.1039/C8TB01421C](https://doi.org/10.1039/C8TB01421C).

851 **Gouw IRTH**, Vlugter IRJC. Physical Properties of Triglycerides III: Ultrasonic Sound Velocity. *Fette,*
852 *Seifen, Anstrichmittel*. 1967; 69(3):159–164. doi: [10.1002/lipi.19670690301](https://doi.org/10.1002/lipi.19670690301).

853 **Gouw TH**, Vlugter JC. Physical Properties of Triglycerides. I. Density and Refractive Index. *Fette,*
854 *Seifen, Anstrichmittel*. 1966; 68(7):544–549. doi: [10.1002/lipi.19660680705](https://doi.org/10.1002/lipi.19660680705).

855 **Guck J**, Ananthakrishnan R, Mahmood H, Moon TJ, Cunningham CC, Käs J. The Optical Stretcher:
856 A Novel Laser Tool to Micromanipulate Cells. *Biophysical Journal*. 2001 Aug; 81(2):767–784. doi:
857 [10.1016/S0006-3495\(01\)75740-2](https://doi.org/10.1016/S0006-3495(01)75740-2).

858 **Guillén-Boixet J**, Kopach A, Holehouse AS, Wittmann S, Jahnel M, Schlüßler R, Kim K, Trussina IREA,
859 Wang J, Mateju D, Poser I, Maharana S, Ruer-Gruß M, Richter D, Zhang X, Chang YT, Guck J, Honig-
860 mann A, Mahamid J, Hyman AA, et al. RNA-Induced Conformational Switching and Clustering of
861 G3BP Drive Stress Granule Assembly by Condensation. *Cell*. 2020 Apr; 181(2):346–361.e17. doi:
862 [10.1016/j.cell.2020.03.049](https://doi.org/10.1016/j.cell.2020.03.049).

863 **Jansen KA**, Donato DM, Balcioğlu HE, Schmidt T, Danen EHJ, Koenderink GH. A Guide to Mechanobi-
864 ology: Where Biology and Physics Meet. *Biochimica et Biophysica Acta (BBA) - Molecular Cell*
865 *Research*. 2015 Nov; 1853(11, Part B):3043–3052. doi: [10.1016/j.bbamcr.2015.05.007](https://doi.org/10.1016/j.bbamcr.2015.05.007).

866 **Jawerth LM**. Salt-Dependent Rheology and Surface Tension of Protein Condensates Using Optical
867 Traps. *Physical Review Letters*. 2018; 121(25). doi: [10.1103/PhysRevLett.121.258101](https://doi.org/10.1103/PhysRevLett.121.258101).

868 **Kim K**, Guck J. The Relative Densities of Cytoplasm and Nuclear Compartments Are Robust against
869 Strong Perturbation. *Biophysical Journal*. 2020 Oct; doi: [10.1016/j.bpj.2020.08.044](https://doi.org/10.1016/j.bpj.2020.08.044).

870 **Kim K**, Yoon H, Diez-Silva M, Dao M, Dasari RR, Park Y. High-Resolution Three-Dimensional Im-
871 aging of Red Blood Cells Parasitized by *Plasmodium Falciparum* and *in Situ* Hemozoin Crystals Us-
872 ing Optical Diffraction Tomography. *Journal of Biomedical Optics*. 2014; 19(1):011005. doi:
873 [10.1117/1.JBO.19.1.011005](https://doi.org/10.1117/1.JBO.19.1.011005).

874 **Kim K**, Yoon J, Shin S, Lee S, Yang SA, Park Y. Optical Diffraction Tomography Techniques for
875 the Study of Cell Pathophysiology. *Journal of Biomedical Photonics & Engineering*. 2016 Jun;
876 2(2):020201. doi: [10.18287/JBPE16.02.020201](https://doi.org/10.18287/JBPE16.02.020201).

877 **Kim M**, Besner S, Ramier A, Kwok SJ, An J, Scarcelli G, Yun SH. Shear Brillouin Light Scattering
878 Microscope. *Optics Express*. 2016 Jan; 24(1):319. doi: [10.1364/OE.24.000319](https://doi.org/10.1364/OE.24.000319).

879 **Koser DE**, Moeendarbary E, Hanne J, Kuerten S, Franze K. CNS Cell Distribution and Axon Ori-
880 entation Determine Local Spinal Cord Mechanical Properties. *Biophysical Journal*. 2015 May;
881 108(9):2137–2147. doi: [10.1016/j.bpj.2015.03.039](https://doi.org/10.1016/j.bpj.2015.03.039).

882 **Kroschwitz S**, Maharana S, Mateju D, Malinovska L, Nüske E, Poser I, Richter D, Alberti S. Promis-
883 cuous Interactions and Protein Disaggregases Determine the Material State of Stress-Inducible
884 RNP Granules. *eLife*. 2015 Aug; 4:e06807. doi: [10.7554/eLife.06807](https://doi.org/10.7554/eLife.06807).

885 **Liaw L**, Prudovsky I, Koza RA, Anunciado-Koza RV, Siviski ME, Lindner V, Friesel RE, Rosen CJ, Baker
886 PRS, Simons B, Vary CPH. Lipid Profiling of In Vitro Cell Models of Adipogenic Differentiation:
887 Relationships With Mouse Adipose Tissues. *Journal of Cellular Biochemistry*. 2016; 117(9):2182–
888 2193. doi: [10.1002/jcb.25522](https://doi.org/10.1002/jcb.25522).

889 **Lieberman AP**, Shakkottai VG, Albin RL. Polyglutamine Repeats in Neurodegenerative Diseases.
890 Annual Review of Pathology: Mechanisms of Disease. 2019; 14(1):1–27. doi: [10.1146/annurev-pathmechdis-012418-012857](https://doi.org/10.1146/annurev-pathmechdis-012418-012857).

892 **Lim J**, Ayoub AB, Antoine EE, Psaltis D. High-Fidelity Optical Diffraction Tomography of Multiple
893 Scattering Samples. *Light: Science & Applications*. 2019 Sep; 8(1):82. doi: [10.1038/s41377-019-0195-1](https://doi.org/10.1038/s41377-019-0195-1).

895 **Litvinov RI**, Shuman H, Bennett JS, Weisel JW. Binding Strength and Activation State of Single
896 Fibrinogen-Integrin Pairs on Living Cells. *Proceedings of the National Academy of Sciences*. 2002
897 May; 99(11):7426–7431. doi: [10.1073/pnas.112194999](https://doi.org/10.1073/pnas.112194999).

898 **Liu L**, Plawinski L, Durrieu MC, Audoin B. Label-Free Multi-Parametric Imaging of Single Cells: Dual
899 Picosecond Optoacoustic Microscopy. *Journal of Biophotonics*. 2019; 12(8):e201900045. doi:
900 [10.1002/jbio.201900045](https://doi.org/10.1002/jbio.201900045).

901 **Lo CM**, Wang HB, Dembo M, Wang YL. Cell Movement Is Guided by the Rigidity of the Substrate.
902 *Biophysical Journal*. 2000 Jul; 79(1):144–152.

903 **Maître JL**, Berthoumieux H, Krens SFG, Salbreux G, Jülicher F, Paluch E, Heisenberg CP. Adhesion
904 Functions in Cell Sorting by Mechanically Coupling the Cortices of Adhering Cells. *Science*. 2012
905 Oct; 338(6104):253–256. doi: [10.1126/science.1225399](https://doi.org/10.1126/science.1225399).

906 **Mammoto T**, Mammoto A, Ingber DE. Mechanobiology and Developmental Control. *Annual Review
907 of Cell and Developmental Biology*. 2013; 29(1):27–61. doi: [10.1146/annurev-cellbio-101512-122340](https://doi.org/10.1146/annurev-cellbio-101512-122340).

909 **Mashaghi A**, Swann M, Popplewell J, Textor M, Reimhult E. Optical Anisotropy of Supported
910 Lipid Structures Probed by Waveguide Spectroscopy and Its Application to Study of Supported
911 Lipid Bilayer Formation Kinetics. *Analytical Chemistry*. 2008 May; 80(10):3666–3676. doi:
912 [10.1021/ac800027s](https://doi.org/10.1021/ac800027s).

913 **Mattana S**, Mattarelli M, Urbanelli L, Sagini K, Emiliani C, Serra MD, Fioretto D, Caponi S. Non-
914 Contact Mechanical and Chemical Analysis of Single Living Cells by Microspectroscopic Tech-
915 niques. *Light: Science & Applications*. 2018 Feb; 7(2):17139–17139. doi: [10.1038/lsa.2017.139](https://doi.org/10.1038/lsa.2017.139).

916 **McCall PM**, Kim K, Fritsch AW, Iglesias-Artola JM, Jawerth LM, Wang J, Ruer M, Peychl J,
917 Poznyakovskiy A, Guck J, Alberti S, Hyman AA, Brugués J. Quantitative Phase Microscopy En-
918 ables Precise and Efficient Determination of Biomolecular Condensate Composition. *bioRxiv*.
919 2020 Oct; p. 2020.10.25.352823. doi: [10.1101/2020.10.25.352823](https://doi.org/10.1101/2020.10.25.352823).

920 **Meichner C**, Schedl AE, Neuber C, Kreger K, Schmidt HW, Kador L. Refractive-Index Determination
921 of Solids from First- and Second-Order Critical Diffraction Angles of Periodic Surface Patterns.
922 *AIP Advances*. 2015 Aug; 5(8):087135. doi: [10.1063/1.4928654](https://doi.org/10.1063/1.4928654).

923 **Meng Z**, Traverso AJ, Yakovlev VV. Background Clean-up in Brillouin Microspectroscopy of Scatter-
924 ing Medium. *Optics Express*. 2014 Mar; 22(5):5410–5415. doi: [10.1364/OE.22.005410](https://doi.org/10.1364/OE.22.005410).

925 **Mohammed D**, Versaevel M, Bruyère C, Alaimo L, Luciano M, Vercruyse E, Procès A, Gabriele S.
926 Innovative Tools for Mechanobiology: Unraveling Outside-In and Inside-Out Mechanotransduc-
927 tion. *Frontiers in Bioengineering and Biotechnology*. 2019; 7. doi: [10.3389/fbioe.2019.00162](https://doi.org/10.3389/fbioe.2019.00162).

928 Müller P, Schürmann M, Guck J. The Theory of Diffraction Tomography. arXiv:150700466 [physics, 929 q-bio]. 2016 Oct; .

930 Nikolić M, Scarcelli G. Long-Term Brillouin Imaging of Live Cells with Reduced Absorption-Mediated 931 Damage at 660 nm Wavelength. *Biomedical Optics Express*. 2019 Mar; 10(4):1567–1580. doi: 932 [10.1364/BOE.10.001567](https://doi.org/10.1364/BOE.10.001567).

933 Norrbacka S, Lindholm D, Myöhänen TT. Prolyl Oligopeptidase Inhibition Reduces PolyQ Aggregation 934 and Improves Cell Viability in Cellular Model of Huntington’s Disease. *Journal of Cellular and Molecular Medicine*. 2019 Dec; 23(12):8511–8515. doi: [10.1111/jcmm.14675](https://doi.org/10.1111/jcmm.14675).

936 Nötzel M, Rosso G, Möllmert S, Seifert A, Schlüßler R, Kim K, Hermann A, Guck J. Axonal Transport, 937 Phase-Separated Compartments and Neuron Mechanics — a New Approach to Investigate 938 Neurodegenerative Diseases. *Frontiers in Cellular Neuroscience*. 2018; 12. doi: [10.3389/fncel.2018.00358](https://doi.org/10.3389/fncel.2018.00358).

940 Oh S, Lee C, Yang W, Li A, Ran C, Yin W, Tabin CJ, Fu D, Xie XS, Kirschner MW. In Situ Measurement 941 of Absolute Concentrations by Normalized Raman Imaging. *bioRxiv*. 2019 May; p. 629543. doi: 942 [10.1101/629543](https://doi.org/10.1101/629543).

943 Patel A, Lee HO, Jawerth L, Maharana S, Jahnel M, Hein MY, Stoynov S, Mahamid J, Saha S, Franz- 944 mann TM, Pozniakovski A, Poser I, Maghelli N, Royer LA, Weigert M, Myers EW, Grill S, Drechsel 945 D, Hyman AA, Alberti S. A Liquid-to-Solid Phase Transition of the ALS Protein FUS Accelerated by 946 Disease Mutation. *Cell*. 2015 Aug; 162(5):1066–1077. doi: [10.1016/j.cell.2015.07.047](https://doi.org/10.1016/j.cell.2015.07.047).

947 Popescu G, Park Y, Lue N, Best-Popescu C, Deflores L, Dasari RR, Feld MS, Badizadegan K. Optical 948 Imaging of Cell Mass and Growth Dynamics. *American Journal of Physiology - Cell Physiology*. 949 2008 Jun; 295(2):C538–C544.

950 Prevedel R, Diz-Muñoz A, Ruocco G, Antonacci G. Brillouin Microscopy: An Emerging Tool for 951 Mechanobiology. *Nature Methods*. 2019 Oct; 16(10):969–977. doi: [10.1038/s41592-019-0543-3](https://doi.org/10.1038/s41592-019-0543-3).

952 Provenzano PP, Eliceiri KW, Campbell JM, Inman DR, White JG, Keely PJ. Collagen Reorganization 953 at the Tumor-Stromal Interface Facilitates Local Invasion. *BMC medicine*. 2006 Dec; 4(1):38. doi: 954 [10.1186/1741-7015-4-38](https://doi.org/10.1186/1741-7015-4-38).

955 Rahman MFA, Arshad MR, Manaf AA, Yaacob MIH. An Investigation on the Behaviour of PDMS as 956 a Membrane Material for Underwater Acoustic Sensing. *IJMS* Vol41(6) [December 2012]. 2012 957 Dec; .

958 Remer I, Shaashoua R, Shemesh N, Ben-Zvi A, Bilenca A. High-Sensitivity and High-Specificity 959 Biomechanical Imaging by Stimulated Brillouin Scattering Microscopy. *Nature Methods*. 2020 960 Aug; 17(9):913–916. doi: [10.1038/s41592-020-0882-0](https://doi.org/10.1038/s41592-020-0882-0).

961 Scarcelli G, Kim P, Yun SH. *In Vivo* Measurement of Age-Related Stiffening in the Crystalline 962 Lens by Brillouin Optical Microscopy. *Biophysical Journal*. 2011; 101(6):1539–1545. doi: 963 <http://dx.doi.org/10.1016/j.bpj.2011.08.008>.

964 Scarcelli G, Pineda R, Yun SH. Brillouin Optical Microscopy for Corneal Biomechanics. *Investigative 965 Ophthalmology & Visual Science*. 2012 Jan; 53(1):185–190. doi: [10.1167/iovs.11-8281](https://doi.org/10.1167/iovs.11-8281).

966 Scarcelli G, Polacheck WJ, Nia HT, Patel K, Grodzinsky AJ, Kamm RD, Yun SH. Noncontact Three- 967 Dimensional Mapping of Intracellular Hydromechanical Properties by Brillouin Microscopy. *Nature Methods*. 2015 Oct; 12:1132.

969 Scarcelli G, Yun SH. Confocal Brillouin Microscopy for Three-Dimensional Mechanical Imaging. 970 *Nature Photonics*. 2008 Jan; 2(1):39–43. doi: [10.1038/nphoton.2007.250](https://doi.org/10.1038/nphoton.2007.250).

971 **Scarcelli G**, Yun SH. Multistage VIPA Etalons for High-Extinction Parallel Brillouin Spectroscopy.
972 *Optics Express*. 2011 May; 19(11):10913–22.

973 **Scarcelli G**, Yun SH. Reply to 'Water Content, Not Stiffness, Dominates Brillouin Spectroscopy
974 Measurements in Hydrated Materials'. *Nature Methods*. 2018 Aug; 15(8):562–563. doi:
975 10.1038/s41592-018-0075-2.

976 **Schlüßler R**, Möllmert S, Abuhattum S, Cojoc G, Müller P, Kim K, Möckel C, Zimmermann C, Czarske
977 J, Guck J. Mechanical Mapping of Spinal Cord Growth and Repair in Living Zebrafish Larvae by
978 Brillouin Imaging. *Biophysical Journal*. 2018 Aug; doi: [10.1016/j.bpj.2018.07.027](https://doi.org/10.1016/j.bpj.2018.07.027).

979 **Schürmann M**, Scholze J, Müller P, Guck J, Chan CJ. Cell Nuclei Have Lower Refractive Index
980 and Mass Density than Cytoplasm. *Journal of Biophotonics*. 2016; 9(10):1068–1076. doi:
981 [10.1002/jbio.201500273](https://doi.org/10.1002/jbio.201500273).

982 **Su JW**, Hsu WC, Tjiu JW, Chiang CP, Huang CW, Sung KB. Investigation of Influences of the
983 Paraformaldehyde Fixation and Paraffin Embedding Removal Process on Refractive Indices and
984 Scattering Properties of Epithelial Cells. *Journal of Biomedical Optics*. 2014 Jul; 19(7):075007. doi:
985 [10.1117/1.JBO.19.7.075007](https://doi.org/10.1117/1.JBO.19.7.075007).

986 **Sung Y**, Choi W, Fang-Yen C, Badizadegan K, Dasari RR, Feld MS. Optical Diffraction Tomog-
987 raphy for High Resolution Live Cell Imaging. *Optics Express*. 2009 Jan; 17(1):266–277. doi:
988 [10.1364/OE.17.000266](https://doi.org/10.1364/OE.17.000266).

989 **Theisen A**. Refractive Increment Data-Book for Polymer and Biomolecular Scientists. Nottingham:
990 Nottingham University Press; 2000.

991 **Traverso AJ**, Thompson JV, Steelman ZA, Meng Z, Scully MO, Yakovlev VV. Dual Raman-Brillouin
992 Microscope for Chemical and Mechanical Characterization and Imaging. *Analytical Chemistry*.
993 2015 Aug; 87(15):7519–7523. doi: [10.1021/acs.analchem.5b02104](https://doi.org/10.1021/acs.analchem.5b02104).

994 **Wabitsch M**, Brenner R, Melzner I, Braun M, Möller P, Heinze E, Debatin KM, Hauner H. Charac-
995 terization of a Human Preadipocyte Cell Strain with High Capacity for Adipose Differentiation.
996 *International Journal of Obesity*. 2001 Jan; 25(1):8–15. doi: [10.1038/sj.ijo.0801520](https://doi.org/10.1038/sj.ijo.0801520).

997 **Wachsmuth M**, Waldeck W, Langowski J. Anomalous Diffusion of Fluorescent Probes in-
998 side Living Cell Nuclei Investigated by Spatially-Resolved Fluorescence Correlation spec-
999 troscopy¹¹Edited by W. Baumeister. *Journal of Molecular Biology*. 2000 May; 298(4):677–689.
1000 doi: [10.1006/jmbi.2000.3692](https://doi.org/10.1006/jmbi.2000.3692).

1001 **Wang C**, Moyses HW, Grier DG. Stimulus-Responsive Colloidal Sensors with Fast Holographic Read-
1002 out. *Applied Physics Letters*. 2015 Aug; 107(5):051903. doi: [10.1063/1.4928178](https://doi.org/10.1063/1.4928178).

1003 **Wu PH**, Aroush DRB, Asnacios A, Chen WC, Dokukin ME, Doss BL, Durand-Smet P, Ekpenyong A,
1004 Guck J, Guz NV, Janmey PA, Lee JSH, Moore NM, Ott A, Poh YC, Ros R, Sander M, Sokolov I,
1005 Staunton JR, Wang N, et al. A Comparison of Methods to Assess Cell Mechanical Properties.
1006 *Nature Methods*. 2018 Jul; 15(7):491–498. doi: 10.1038/s41592-018-0015-1.

1007 **Wu PJ**, Kabakova I, Ruberti J, Sherwood JM, Dunlop IE, Paterson C, Török P, Overby DR. Brillouin Mi-
1008 croscopy, What Is It Really Measuring? arXiv:171103312v2 [q-bioQM]. 2018; doi: [10.1038/s41592-018-0076-1](https://doi.org/10.1038/s41592-018-0076-1).

1009 **Wu PJ**, Kabakova IV, Ruberti JW, Sherwood JM, Dunlop IE, Paterson C, Török P, Overby DR. Water
1010 Content, Not Stiffness, Dominates Brillouin Spectroscopy Measurements in Hydrated Materials.
1011 *Nature Methods*. 2018 Aug; 15(8):561–562. doi: [10.1038/s41592-018-0076-1](https://doi.org/10.1038/s41592-018-0076-1).

¹⁰¹³ **Yang J**, Yang X. Phase Transition of Huntingtin: Factors and Pathological Relevance. *Frontiers in Genetics*. 2020; 11. doi: [10.3389/fgene.2020.00754](https://doi.org/10.3389/fgene.2020.00754).

¹⁰¹⁵ **Zangle TA**, Teitel MA. Live-Cell Mass Profiling: An Emerging Approach in Quantitative Biophysics. ¹⁰¹⁶ *Nat Meth*. 2014 Dec; 11(12):1221-1228.

¹⁰¹⁷ **Zhao H**, Brown PH, Schuck P. On the Distribution of Protein Refractive Index Increments. *Biophysical Journal*. 2011 May; 100(9):2309-2317. doi: [10.1016/j.bpj.2011.03.004](https://doi.org/10.1016/j.bpj.2011.03.004).

¹⁰¹⁹ **Zouani OF**, Dehoux T, Durrieu MC, Audoin B. Universality of the Network-Dynamics of the Cell Nucleus at High Frequencies. *Soft Matter*. 2014 Oct; 10(43):8737-8743. doi: [10.1039/C4SM00933A](https://doi.org/10.1039/C4SM00933A).

¹⁰²¹ **Acknowledgements**

¹⁰²² We thank Anthony Hyman from the Max Planck Institute of Molecular Cell Biology and ¹⁰²³ Genetics for providing the stable HeLa cell lines, Prof. Martin Wabitsch from the Cen-¹⁰²⁴ tre for Hormonal Disorders in Children and Adolescents – Ulm University Hospital for ¹⁰²⁵ providing the SGBS preadipocytes, and the Center for Molecular and Cellular Bioengi-¹⁰²⁶ neering Light Microscopy Facility (partly funded by the State of Saxony and the European ¹⁰²⁷ Fund for Regional Development - EFRE) for technical support. Financial support from ¹⁰²⁸ the Deutsche Forschungsgemeinschaft (SPP 2191 – Molecular mechanisms of functional ¹⁰²⁹ phase separation, grant agreement number 419138906 to S.Al. and J.G.), Volkswagen ¹⁰³⁰ Stiftung (grant agreement number 92847 to S.Al. and J.G.), the Alexander von Humboldt-¹⁰³¹ Stiftung (Alexander von Humboldt-Professorship to J.G.) are gratefully acknowledged. ¹⁰³² A.H. is supported by the NOMIS foundation and the Hermann und Lilly Schilling-Stiftung ¹⁰³³ für medizinische Forschung im Stifterverband.

¹⁰³⁴ **Additional information**

¹⁰³⁵ **Competing financial interests** The authors declare no competing financial interests.